Mon. Not. R. Astron. Soc. **000**, 000–000 (0000) Printed 4 October 2013 (MN LATEX style file v2.2)

Tidal resonance locks in inspiraling white dwarf binaries

Joshua Burkart,[1] Eliot Quataert,[1,2] Phil Arras,[3] and Nevin N. Weinberg[4]

[1]*Department of Physics, 366 LeConte Hall, University of California, Berkeley, CA 94720, USA*
[2]*Department of Astronomy & Theoretical Astrophysics Center, 601 Campbell Hall, University of California Berkeley, CA 94720, USA*
[3]*Department of Astronomy, University of Virginia, P.O. Box 400325, Charlottesville, VA 22904-4325, USA*
[4]*Department of Physics and MIT Kavli Institute, MIT, 77 Massachusetts Avenue, Cambridge, MA 02139, USA*

Accepted to MNRAS

ABSTRACT

We calculate the tidal response of helium and carbon/oxygen (C/O) white dwarf (WD) binaries inspiraling due to gravitational wave emission. We show that resonance locks, previously considered in binaries with an early-type star, occur universally in WD binaries. In a resonance lock, the orbital and spin frequencies evolve in lockstep, so that the tidal forcing frequency is approximately constant and a particular normal mode remains resonant, producing efficient tidal dissipation and nearly synchronous rotation. We show that analogous locks between the spin and orbital frequencies can occur not only with global standing modes, but even when damping is so efficient that the resonant tidal response becomes a traveling wave. We derive simple analytic formulas for the tidal quality factor $\mathcal{Q}_{\rm t}$ and tidal heating rate during a g-mode resonance lock, and verify our results numerically. We find that $\mathcal{Q}_{\rm t} \sim 10^7$ for orbital periods $\lesssim 1-2$ hr in C/O WDs, and $\mathcal{Q}_{\rm t} \sim 10^9$ for $P_{\rm orb} \lesssim 3-10$ hr in helium WDs. Typically tidal heating occurs sufficiently close to the surface that the energy should be observable as surface emission. Moreover, near an orbital period of ~ 10 min, the tidal heating rate reaches $\sim 10^{-2} L_\odot$, rivaling the luminosities of our fiducial WD models. Recent observations of the 13-minute double-WD binary J0651 are roughly consistent with our theoretical predictions. Tides naturally tend to generate differential rotation; however, we show that the fossil magnetic field strength of a typical WD can maintain solid-body rotation down to at least $P_{\rm orb} \sim 10$ min even in the presence of a tidal torque concentrated near the WD surface.

Key words: binaries, white dwarfs, waves, instabilities

1 INTRODUCTION

In this work, we consider the effect of tides in detached white dwarf (WD) binaries inspiraling due to energy and angular momentum loss by gravitational waves. Our analysis is motivated by several important questions. For example, to what degree should short-period WD binaries exhibit synchronized rotational and orbital motion? Should WDs in close binaries be systematically hotter than their isolated counterparts, as a result of tidal dissipation? What is the thermal state of WDs prior to the onset of mass transfer?

Several past studies have applied linear perturbation theory to the problem considered in this work. Campbell (1984) and Iben et al. (1998) applied the theory of the equilibrium tide to WD binaries, using parameterized viscosities to estimate the tidal torque. Willems et al. (2010) considered turbulent convective damping acting on the equilibrium tide, as originally considered by Zahn (1977) for late-type stars, and showed that this effect is not able to synchronize a WD binary within its gravitational wave inspiral time.

Rathore et al. (2005) and Fuller & Lai (2011) moved beyond the large-scale, nonresonant equilibrium tide, and considered the tidal excitation of standing g-modes during inspiral, analyzing the behavior of wave amplitudes as a system sweeps through resonances. However, neither study allowed the WD's spin rate to evolve, an assumption that eliminated the physics highlighted in this work.

In this paper we also focus on tidally excited g-modes in WD binaries; one of our goals is to assess whether the resonantly excited "dynamical tide" represents a traveling or standing wave. This amounts to whether a tidally generated wave is able to reflect at its inner and outer radial turning points. If reflection cannot occur, then a damping time of order the group travel time across the mode propagation cavity results; if reflection does occur, then the wave amplitude can build up significantly during close resonances between g-mode frequencies and the tidal forcing frequency.

This question has been addressed before in the context of main-sequence stars. Zahn (1975) employed a traveling wave description of the dynamical tide in the context of early-type stars with radiative envelopes, assuming waves would be absorbed near the surface by rapid radiative diffusion. Goldreich & Nicholson (1989a) enhanced this argument, showing that dynamical tides first cause tidal synchronization in such a star's outer regions, leading to the development of critical layers and even stronger radiative damping. However, they did not assess whether angular momentum

redistribution could enforce solid-body rotation and thereby eliminate critical layers; we address this important point in § 6.2. In the absence of critical layers, Witte & Savonije (1999) introduced the phenomenon of resonance locks (§ 4), which rely on the large wave amplitudes produced during eigenmode resonances. We will show that similar resonance locks occur ubiquitously in close WD binaries.

Goodman & Dickson (1998) considered the case of late-type stars with convective envelopes, and showed that tidally generated waves excited at the edge of the convection zone steepen and break near the cores of such stars. Fuller & Lai (2012), in their study of the tidal evolution of WD binaries, found that the dynamical tide in a carbon/oxygen WD instead breaks near the outer turning point. As such, they invoked an outgoing-wave boundary condition in their analysis. We find that their assumption may not be generally applicable due to an overestimate of the degree of wave breaking; see § 6.1. As a result the dynamical tide may represent a standing wave for a substantial portion of a WD binary's inspiral epoch.

This paper is organized as follows. In § 2 we provide pertinent background information on WDs and tidal effects that our subsequent results rely on. In § 3 we give a broad overview of the results we derive in more detail in §§ 4 – 8. In § 4 we consider the case of resonance locks created by standing waves. We analyze the resulting tidal efficiency and energetics in § 5. In § 6 we analyze whether standing waves are able to occur, considering wave breaking in § 6.1 and critical layers in § 6.2. In § 7 we turn our attention to traveling waves, discussing wave excitation and interference in § 7.1 and showing that traveling waves can also create resonance locks in § 7.2. In § 8 we then employ numerical simulations to combine our standing and traveling wave results. In § 9 we compare our results to observational constraints and discuss physical effects that need to be considered in future work. We then conclude in § 10 with a summary of our salient results.

2 BACKGROUND

A short-period compact object binary efficiently emits gravitational waves that carry off energy and angular momentum. This process causes its orbit to circularize; as such, we will restrict our attention to circular WD binaries in this work (however, see Thompson 2011). Gravitational waves also cause such a binary's orbit to decay according to $\dot{\Omega} = \Omega/t_{\rm gw}$, where the characteristic gravitational wave inspiral timescale for a circular orbit is (Peters 1964)

$$t_{\rm gw} = \omega_*^{-1} \frac{5}{96} \frac{\left(1+M'/M\right)^{1/3}}{M'/M} \beta_*^{-5} \left(\frac{\omega_*}{\Omega}\right)^{8/3}. \qquad (1)$$

Here $\omega_*^2 = GM/R^3$ is the dynamical frequency of the primary, M' is the mass of the companion, $\beta_*^2 = GM/Rc^2$ is the relativity parameter of the primary, and Ω is the orbital frequency. The time a binary will take until it begins to transfer mass is given by $t_{\rm merge} = 3t_{\rm gw}/8$. For a $0.6M_\odot$ WD with an equal-mass companion, orbital periods of less than ~ 530 min imply the binary will begin mass transfer within 10 Gyr; this restriction reduces to $P_{\rm orb} \lesssim 270$ min for a $0.2M_\odot$ WD with an equal-mass companion.

During the process of inspiral, the tidal force acting on each element of the binary steadily grows. The tidal response on a star is typically divided conceptually into two components: the equilibrium tide and the dynamical tide. The equilibrium tide represents the large-scale distortion of a star by a companion's tidal force (Zahn 1977); it is often theoretically modeled as the filling of an equipotential surface, but can also be treated as the collective non-resonant response of all of a star's eigenmodes. The two viewpoints are equivalent, as in both the tidal forcing frequency is set to zero. Except near very strong resonances, the equilibrium tide contains the great majority of the tidal energy. Nonetheless, whether it produces a strong torque is also influenced by the degree to which it lags behind the tidal potential, which is determined by how strongly

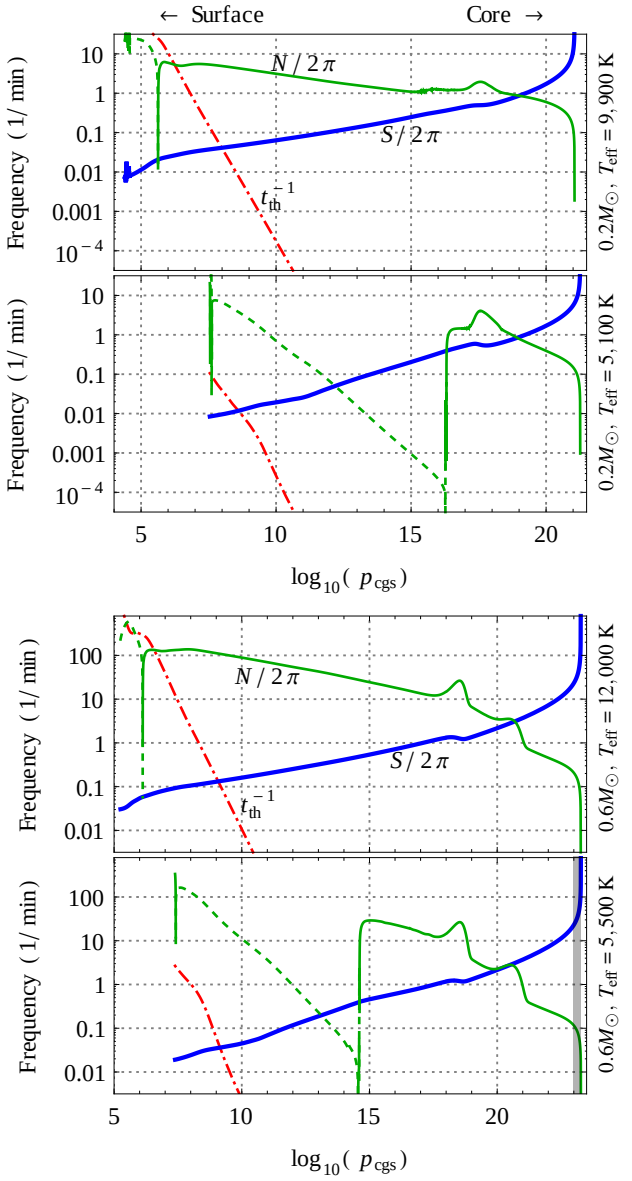

Figure 1. Propagation diagrams for several of our WD models listed in Table 1. The top two panels are our $0.2M_\odot$ `He10` and `He5` helium WDs, with $T_{\rm eff} = 9,900$ and 5,100 K respectively; the bottom two panels are our $0.6M_\odot$ `CO12` and `CO6` carbon/oxygen WDs, with $T_{\rm eff} = 12,000$ and 5,500 K respectively. Each plot shows the Brunt-Väisälä frequency N (green line; dashed indicates $N^2 < 0$), the quadrupolar Lamb frequency S (thick blue line), and inverse local thermal time $1/t_{\rm th} = gF/pc_pT$ (red dot-dashed line). A g-mode is able to propagate where its frequency is less than both N and S. In the bottom panel showing our `CO6` model, the shaded region at high pressure indicates the plasma interaction parameter $\Gamma > 220$, implying crystallization occurs (which is not included in our model); see § 9.3.

Table 1. WD models. Masses of the helium models (top three) are $0.2M_\odot$; masses of the carbon/oxygen models (bottom two) are $0.6M_\odot$. Helium models each have a hydrogen layer of mass $0.0033M$, and were generated with MESA (Paxton et al. 2011); carbon/oxygen models each have a helium layer of mass $0.017M$ and a hydrogen layer of mass $0.0017M$. Further details on white dwarf models are given in Appendix D; Figure 1 provides propagation diagrams for several models. The dynamical time is $t_*^2 = R^3/GM$; the thermal time at the radiative-convective boundary (RCB) is $t_{\rm th}|_{\rm rcb} = pc_pT/gF|_{\rm rcb}$, where we take $2\pi/N = 100$ min to define the RCB; the WD cooling time is $t_{\rm cool} = E_{\rm th}/L$, where $E_{\rm th} = \int c_pT\,dM$ approximates the total thermal energy; $M_{\rm conv}$ is the mass in the outer convection zone, which increases in size by many orders of magnitude as a WD cools (see Figure 1); the plasma interaction parameter at the center of the WD is $\Gamma_{\rm core} = Z^2e^2/kTd_{\rm i}|_{r=0}$, where Ze is the mean ion charge, $d_{\rm i}$ is the ion spacing, and the value of Γ corresponding to the onset of crystallization is discussed in § 9.3; the relativity parameter is $\beta_*^2 = GM/Rc^2$; and I_* is the WD moment of inertia.

ID	$T_{\rm eff}$ (K)	$L/L_\odot$	$R/R_\odot$	t_* (sec)	$t_{\rm th}\|_{\rm rcb}$ (yr)	$t_{\rm cool}$ (Gyr)	$M_{\rm conv}/M$	$\Gamma_{\rm core}$	$\beta_*/10^{-2}$	I_*/MR^2
He10	9,900	1.3×10^{-2}	0.038	26.	7.7×10^{-8}	0.36	3×10^{-14}	1.2	0.34	0.085
He7	7,000	1.9×10^{-3}	0.029	18.	5.1×10^{1}	0.98	1×10^{-7}	2.7	0.38	0.11
He5	5,100	3.9×10^{-4}	0.025	14.	1.3×10^{6}	2.5	2×10^{-4}	5.1	0.41	0.14
CO12	12,000	3.0×10^{-3}	0.013	3.1	6.5×10^{-9}	0.59	1×10^{-16}	71.	0.99	0.16
CO6	5,500	1.3×10^{-4}	0.013	2.9	7.3×10^{2}	4.5	3×10^{-8}	260.	1.0	0.18

the equilibrium tide is damped. For WDs, Willems et al. (2010) showed that turbulent convection acting on the equilibrium tide does not cause significant synchronization (Appendix B2).

The dynamical tide, on the other hand, corresponds to the tidal excitation of internal stellar waves (Zahn 1975). In particular, given that tidal forcing periods are much longer than the stellar dynamical timescale, buoyancy-supported gravity waves or g-modes are predominantly excited (although rotationally supported modes become important when the rotation and tidal forcing frequencies become comparable; see § 9.2). Propagation of gravity waves is primarily determined by the Brunt-Väisälä frequency N, given by

$$N^2 = \frac{1}{g}\left(\frac{1}{\Gamma_1}\frac{d\ln p}{dr} - \frac{d\ln\rho}{dr}\right), \tag{2}$$

where Γ_1 is the adiabatic index. A g-mode is able to propagate where its frequency lies below both N as well as the Lamb frequency $S_l^2 = l(l+1)c_{\rm s}^2/r^2$. Plots of both N and S_l for several helium and carbon/oxygen WD models are provided in Figure 1.

Degeneracy pressure satisfies $p \propto \rho^{\Gamma_1}$; substituting this into equation (2) yields $N = 0$. Thus the Brunt-Väisälä frequency becomes very small in the WD core where degeneracy pressure dominates gas pressure, scaling as $N^2 \propto kT/E_{\rm F}$, where $E_{\rm F}$ is the Fermi energy. Moreover, WDs also often possess outer convection zones with $N^2 < 0$. As a result, a typical tidally excited g-mode in a WD possesses both an inner turning point near the core as well as an outer turning point near the radiative-convective boundary.

Lastly, temporarily ignoring degeneracy pressure and assuming an ideal gas equation of state, equation (2) can be expressed as (Hansen et al. 2004)

$$N^2 = \frac{\nabla_{\rm ad}\rho^2g^2c_pT}{p^2}(\nabla_{\rm ad} - \nabla) - g\frac{d\ln\mu}{dr}, \tag{3}$$

where μ is the mean molecular weight. From this expression we can see that the Brunt-Väisälä frequency becomes larger in composition gradient zones, where μ decreases with radius. This can be seen in Figure 1, where a "bump" in N occurs in helium models due to the helium to hydrogen transition; two bumps are present in carbon/oxygen models, resulting from carbon/oxygen → helium and helium → hydrogen.

3 DYNAMICAL TIDE REGIMES IN WHITE DWARFS

Here we will give a general overview of the results covered in §§ 4 – 8 by enumerating four essential regimes of the dynamical tide in WDs, which comprises the wavelike tidal response. The two basic distinctions made by our four regimes are a) whether tidally excited gravity waves can reflect and become large-amplitude standing modes, or whether they instead represent traveling waves; and b) whether or not a resonance lock can be created. Resonance locks are described in detail in §§ 4 & 7.2; they occur when the tidal torque causes the tidal forcing frequency $\sigma = 2(\Omega - \Omega_{\rm spin})$ to remain constant even as the orbit shrinks.

First, the two regimes where standing waves exclusively occur are:

S1) In this regime the dynamical tide represents a purely standing wave, but with a resulting torque that is insufficient to effect a resonance lock even during a perfect resonance. This occurs for long orbital periods or small companion masses. As such, the system quickly sweeps through resonances, and the time-averaged torque is dominated by its value away from resonances. This nonresonant torque is proportional to the eigenmode damping rate, and is thus very small for WDs, due to their long thermal times. As a consequence the average tidal quality factor is very large, tidal heating is negligible, and the spin rate remains essentially constant.

S2) Here the dynamical tide is again a standing wave, but with eigenmode amplitudes large enough to create resonance locks. This regime is addressed in detail in § 4; we estimate the orbital period corresponding to its onset in equation (10). During a resonance lock, tides become efficient: due to strong tidal torques, the spin frequency changes at the same rate as the orbit decays due to gravitation wave emission. Definite predictions result for the tidal energy deposition rate (equation 20) and tidal quality factor (equation 17).

Next, the regimes strongly influenced by traveling waves are:

T1) In this regime, the off-resonance dynamical tide is still a standing wave, but near resonances the wave amplitude becomes so large that reflection near the surface cannot occur due to wave breaking (§ 6.1). Furthermore, the traveling wave torque is too weak to cause a resonance lock. Since the typical torque experienced by the WD is once again the off-resonance standing wave value, the synchronization and tidal heating scenario is very similar to regime (S1)—in other words, tides are ineffective.

T2) Just as with regime (T1), the standing wave torque is capped at resonances, becoming a traveling wave; however in this regime the traveling wave torque itself is strong enough to create a resonance lock (terminology discussed further in footnote 5), as addressed in § 7. We estimate the onset of this regime in equation (33).

The predictions for the tidal energy deposition rate and quality factor are the same as in (S2).

Although we consider only these four regimes in this work, at shorter orbital periods and nearly synchronous rotation, physical effects such as Coriolis modification of stellar eigenmodes and nonlinear tidal excitation mechanisms are likely to become very important; see § 9.2.

The archetypal scenario is as follows. A WD binary with a sufficiently long orbital period begins in regime (S1). Eventually, as the orbit shrinks due to gravitational radiation and the tidal force correspondingly increases in magnitude, the dynamical tide becomes strong enough that a resonance lock takes effect and regime (S2) is reached. However, as inspiral accelerates, the torque necessary to maintain the resonance lock becomes larger, requiring larger wave amplitudes. When the amplitude becomes too great, the wave begins to break near the outer turning point, and the system enters regime (T1). Finally, when the traveling wave torque becomes large enough to create a resonance lock, it enters regime (T2). In § 8, we verify this picture numerically.

4 RESONANCE LOCKS BY STANDING WAVES

We assume in this section that the dynamical tide is a superposition of standing waves and proceed to predict the tidal evolution of a WD binary. We discuss the applicability of the standing wave limit in § 6.

Assuming a circular orbit and alignment of spin and orbital angular momenta, the secular tidal torque on a star can be expressed as a sum over quadrupolar ($l = 2$) eigenmodes indexed by their number of radial nodes n (Appendix B2):

$$\tau = 8mE_*\varepsilon^2 W^2 \sum_n Q_n^2 \left[\frac{\omega_n^2 \sigma \gamma_n}{(\omega_n^2-\sigma^2)^2+4\sigma^2\gamma_n^2}\right]. \tag{4}$$

Here $\sigma = m(\Omega - \Omega_{\rm spin})$ is the tidal driving frequency in the corotating frame, Ω is the orbital frequency, $\Omega_{\rm spin}$ is the solid-body rotation rate, $m = 2$, $E_* = GM^2/R$ is the WD energy scale, $\varepsilon = (M'/M)(R/a)^3$ is the tidal factor, M' is the companion mass, a is the orbital separation, $W^2 = 3\pi/10$, and γ_n is an eigenmode damping rate (Appendix B3). Our eigenfunction normalization convention is given in equation (B5); physical quantities such as the torque are of course independent of the choice of normalization.

The linear overlap integral Q_n appearing in equation (4) represents the spatial coupling strength of an eigenmode to the tidal potential, and is normalization dependent. Since the tidal potential spatially varies only gradually, Q_n is large for low-order modes, and becomes much smaller for high-order, short-wavelength modes. We describe various methods of computing Q_n in Appendix B4.

The factor in brackets in equation (4) describes the temporal coupling of an eigenmode to the tidal potential, and becomes very large during resonances, when the tidal driving frequency becomes close to a stellar eigenfrequency. The nonresonant limit of this factor, which corresponds to the equilibrium tide, increases with stronger damping. Paradoxically, however, the torque during a resonance is inversely proportional to the damping rate, since damping limits the maximum energy a resonant mode attains.

We note that by invoking steady-state solutions to the mode amplitude equations, as we have done here, we fail to account for the energy and angular momentum transfer required to bring a mode's amplitude up to the steady-state value. Additionally, the steady-state solution itself may fail to model the behavior of mode amplitudes very close to resonances correctly; we address this in § 6.3. Correctly accounting for these two considerations would involve simultaneously solving both the mode amplitude equations for all relevant modes as well as the orbital evolution equations, a task we leave to future study.

Continuing, we focus on resonant tidal effects, and consider the case of a particular eigenmode with a frequency close to the tidal driving frequency, i.e. $\omega_n \approx \sigma$. We can then make this substitution everywhere in equation (4) other than in the detuning frequency $\delta\omega_n = \omega_n - \sigma$ to find

$$\tau \approx 2mE_*\varepsilon^2 W^2 Q_n^2 \left(\frac{\omega_n \gamma_n}{\delta\omega_n^2+\gamma_n^2}\right), \tag{5}$$

having dropped nonresonant terms. One might expect that since the strongest torques are achieved very near resonance, where $\delta\omega_n \sim 0$, a system should evolve quickly through resonances, and they should have little effect on the long-term orbital and spin evolution. This is often accounted for by using a "harmonic mean" of the torque to produce a synchronization time, i.e., $t_{\rm sync} = \int I_* d\Omega/\tau$, where I_* is the moment of inertia (Goodman & Dickson 1998).

Under particular circumstances, however, it is possible to achieve a resonance lock, where an eigenmode remains in a highly resonant state for an extended period of time, as originally proposed by Witte & Savonije (1999). Very near a resonance, the torque depends very strongly on the detuning frequency $\delta\omega_n$, and very weakly on the orbital period by itself; as a result, the essential criterion that must be satisfied for a resonance lock to occur is that the detuning frequency must remain constant:

$$0 = \dot{\delta\omega_n} = m\left((1-C_n)\dot{\Omega}_{\rm spin} - \dot{\Omega}\right), \tag{6}$$

where $\partial\omega_n/\partial\Omega_{\rm spin} = -mC_n$ accounts for rotational modification of the stellar eigenmodes, $C_n \approx 1/6$ for high-order $l = 2$ g-modes and slow rotation (Unno et al. 1989), and we have assumed the WD rotates as a solid body. (We justify the solid-body rotation assumption in § 6.2.)

For simplicity, we will henceforth ignore rotational modification of the stellar eigenfrequencies, so that $C_n \to 0$. This limits the quantitative applicability of our results to where $\Omega - \Omega_{\rm spin} \gtrsim \Omega_{\rm spin}$. We also neglect progressive WD cooling, which decreases the Brunt-Väisälä frequency and consequently lowers eigenmode frequencies; this is valid so long as the cooling time $t_{\rm cool}$, which is on the order of $\sim$ Gyr for the models listed in Table 1, is much longer than the gravitational wave decay time $t_{\rm gw}$ (equation 1). Subject to these simplifications, equation (6) then reduces to $\dot{\Omega} = \dot{\Omega}_{\rm spin}$, i.e., that the orbital and spin frequencies evolve at the same rate. Since the orbital frequency increases due to the emission of gravitational waves, and the spin frequency increases due to tidal synchronization, this phenomenon is plausible at first glance. We now work out the mathematical details.

The evolution of $\Omega_{\rm spin}$ and Ω proceed as

$$\begin{pmatrix}\dot{\Omega}_{\rm spin}/\Omega_{\rm spin} \\ \dot{\Omega}/\Omega\end{pmatrix} = \begin{pmatrix}\tau/I_*\Omega_{\rm spin} \\ 1/t_{\rm gw} + (3/2)(\dot{E}_{\rm tide}/|E_{\rm orb}|)\end{pmatrix}, \tag{7}$$

where $\dot{E}_{\rm tide}$ is the secular tidal energy transfer rate[1] and the gravitational wave inspiral time $t_{\rm gw}$ is given in equation (1). Here we have failed to account for tidal effects in the companion, which would provide an extra contribution to $\dot{E}_{\rm tide}$; see below.

[1] Our convention is that $\tau > 0$ or $\dot{E}_{\rm tide} > 0$ implies that orbital angular momentum or energy is being transfered to the WD(s).

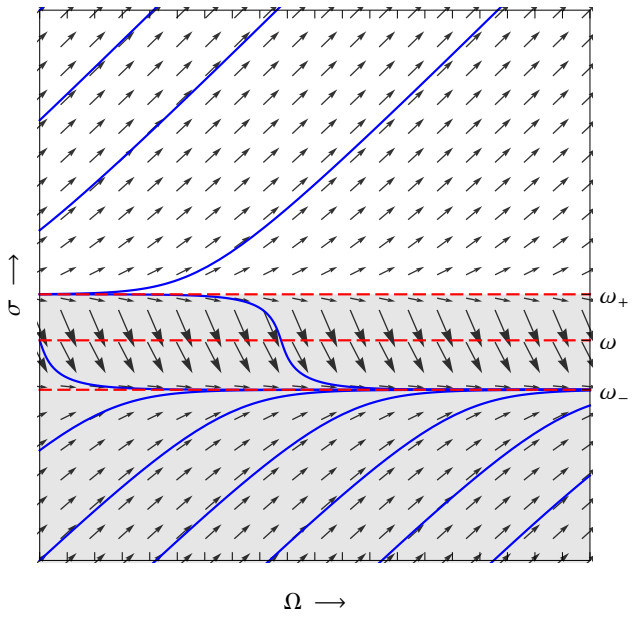

Figure 2. Plot schematically illustrating the dynamics of a resonance lock. The abscissa is the orbital frequency Ω, which increases due to gravitational wave radiation, and the ordinate is the Doppler-shifted $l = m = 2$ tidal driving frequency $\sigma = 2(\Omega - \Omega_{\rm spin})$. The arrows depict the vector field describing the orbital evolution equations (equation 7). The eigenfrequency of the included mode is ω, which is flanked by stable and unstable fixed points of the evolution equations: ω_- and ω_+, respectively. The dashed red horizontal lines show these three frequencies, while the blue curves are example system trajectories. The stable point ω_- corresponds to a resonance lock, while the unstable fixed point ω_+ corresponds to the upper boundary of the stable fixed point's basin of attraction (shaded region). In producing this plot, the correct functional form of the equation of motion has been used, except with $t_{\rm gw}$ and ε taken as constant, and with artificially chosen values of the various germane parameters. In particular, for realistic resonance lock situations in WDs, the three frequencies shown are very close together, and the basin of attraction barely extends beyond ω_-.

Using equations (7) and (B8), equation (6) becomes

$$\frac{\Omega}{t_{\rm gw}} = \tau \left(\frac{1}{I_*} - \frac{3}{2} \frac{1}{\mu a^2} \right), \tag{8}$$

where $\mu = MM'/(M+M')$ is the reduced mass. Since $\mu a^2 \gg I_*$, in the present context we can neglect any tidal influence on $\dot{\Omega}$ even in this extreme-resonance scenario; this also now justifies dropping the companion's contribution to $\dot{E}_{\rm tide}$. We can then approximate the resonance lock criterion as

$$\frac{\Omega}{t_{\rm gw}} = \frac{\tau}{I_*}. \tag{9}$$

This implies that in a resonance lock, the torque increases as $\tau \propto \Omega^{11/3}$ as the orbit decays.

Once equation (9) is satisfied, the lock can persist for a long period of time, since the quantities in equation (5) affecting the magnitude of the torque other than $\delta\omega_n$ change only very gradually in time. (We verify this using numerical orbital evolution simulations in § 8.) In other words, a resonance lock represents a dynamical attractor; Figure 2 provides an illustration of the nonlinear dynamics behind a resonance lock. The lock could eventually be destroyed if the mode responsible began to break near its outer turning point, which would drastically increase the effective damping rate. This phenomenon is explained in § 6.

Table 2. WD tidal parameters. For each of our fiducial WD models from Table 1, we list the orbital period $P_{\rm rl}$ of its first resonance lock (§ 4, equation 10), the orbital period $P_{\rm trl}$ below which traveling wave resonance locks can occur (§ 7.2, equation 33), its value of λ (§ 5, equation 14), and the tidal quality factor $\mathcal{Q}_{\rm t}|_{100\ \rm min}$ for a resonance lock (§ 5.1, equation 17) evaluated at $P_{\rm orb} = 100$ min. All values are for an equal-mass companion. We determined $P_{\rm rl}$ and $P_{\rm trl}$ by directly searching over numerically computed eigenmode properties.

ID	$P_{\rm rl}$ (min)	$P_{\rm trl}$ (min)	$\lambda/10^{-2}$	$\mathcal{Q}_{\rm t}\|_{100\ \rm min}$
He10	67	49	1.2	2×10^9
He7	270	49	2.4	1×10^9
He5	1,400	90	4.6	1×10^9
CO12	31	22	6.3	1×10^7
CO6	170	40	7.4	1×10^7

If we assume that the system begins completely unsynchronized, so that $\sigma = 2\Omega$, we can determine the orbital period where a lock first occurs, which we denote $P_{\rm rl}$, by substituting equations (5) and (1) into (9), setting $\omega_n = \sigma$ and hence $\delta\omega_n = 0$, and then solving for the orbital period. To this end, we invoke the following approximate scalings for the eigenmode linear tidal overlap integral Q and damping rate γ:

$$Q \approx Q_0 (\sigma/\omega_*)^a \quad \text{and} \quad \gamma \approx \gamma_0 (\sigma/\omega_*)^{-b},$$

where values of the various parameters in these expressions are listed in Table 3 for our fiducial WD models. Scaling parameter values to those for our CO6 model, we have

$$P_{\rm rl} \sim 170\ {\rm min} \left(\frac{t_*}{2.9\ {\rm s}} \right) F_{\rm rl}^p, \tag{10}$$

where $t_* = (R^3/GM)^{1/2}$ is the WD's dynamical time, the factor $F_{\rm rl}$ is

$$\begin{aligned} F_{\rm rl} \sim & \left(\frac{M'}{M} \right) \left(\frac{1 + M'/M}{2} \right)^{-5/3} \\ & \times \left(\frac{\beta_*}{0.010} \right)^{-5} \left(\frac{I_*}{0.18 M R^2} \right)^{-1} \\ & \times \left(\frac{Q_0}{27} \right)^2 \left(\frac{\gamma_0}{2.9 \times 10^{-14} \omega_*} \right)^{-1} \\ & \times \left(2.15 \times 10^{26} \right) (0.00327)^{1/p}, \end{aligned} \tag{11}$$

the power p is in general

$$p = \frac{1}{4/3 + 2a + b} \ll 1, \tag{12}$$

and $p = 0.094$ for our CO6 model (Table 3). (The last line of equation 11 is equal to unity for $p = 0.094$.)

For comparison, direct numerical evaluation of eigenmode properties with our CO6 WD model yields $P_{\rm rl} = 170$ min for an equal-mass companion, due to an $n = 122$ g-mode. This is in very good agreement with the analytic approximation in equation (10), and is also consistent with our numerical results in § 8. We provide values of $P_{\rm rl}$ for each of our fiducial models in Table 2. These results show that resonance locks begin at longer orbital periods for cooler WD models, due to larger outer convective zones and longer overall diffusive damping times (smaller γ_n; see Table 3 & Figure B1). This increases the maximum possible tidal torque, which is proportional to $1/\gamma_n$ (equation 5).

5 ENERGETICS

5.1 Tidal quality factor

A star's tidal quality factor $\mathcal{Q}_\mathrm{t}$ can be defined as

$$\mathcal{Q}_\mathrm{t} = \frac{\Omega E_\mathrm{tide}}{\dot{E}_\mathrm{tide}}, \tag{13}$$

where the energy content of the tide E_tide is approximately given by (Appendix B2)

$$E_\mathrm{tide} = \lambda \varepsilon^2 E_*, \tag{14}$$

$\lambda = 2W^2 \sum_n Q_n^2$, and values of λ for various WD models are given in Table 2. Using the relationship between the tidal torque and energy transfer rate from equation (B8), we see that the tidal torque can be expressed in terms of $\mathcal{Q}_\mathrm{t}$ by

$$\tau = \frac{E_\mathrm{tide}}{\mathcal{Q}_\mathrm{t}}. \tag{15}$$

Since $E_\mathrm{tide} \sim \lambda F_\mathrm{tide}\, h$, where $h \sim \varepsilon R$ is the height of the equilibrium tide and $F_\mathrm{tide} \sim \varepsilon E_*/R$ is the tidal force, we see that our definition of $\mathcal{Q}_\mathrm{t}$ is consistent with $1/\mathcal{Q}_\mathrm{t}$ representing an effective tidal lag angle; see e.g. Goldreich & Soter (1966). Note that since $\mathcal{Q}_\mathrm{t}$ parameterizes the total tidal energy deposition rate, which includes mechanical energy transfer associated with increasing the WD spin, the value of $\mathcal{Q}_\mathrm{t}$ alone does not fully determine the tidal heating rate; see § 5.2.

Using the previous three equations along with the resonance lock condition from equation (9), we have that the value of $\mathcal{Q}_\mathrm{t}$ during a resonance lock is

$$\mathcal{Q}_\mathrm{t} = \frac{\lambda \varepsilon^2 t_\mathrm{gw} E_*}{I_* \Omega}. \tag{16}$$

Substituting further yields

$$\begin{aligned}\mathcal{Q}_\mathrm{t} \approx 9.7 \times 10^6 &\left(\frac{P_\mathrm{orb}}{100\ \mathrm{min}}\right)^{-1/3} \left(\frac{t_*}{2.9\ \mathrm{s}}\right)^{1/3} \\ &\times \left(\frac{M'}{M}\right) \left(\frac{1+M'/M}{2}\right)^{-5/3} \left(\frac{\lambda}{0.074}\right) \\ &\times \left(\frac{I_*}{0.18 M R^2}\right)^{-1} \left(\frac{\beta_*}{0.010}\right)^{-5}.\end{aligned} \tag{17}$$

Here I_* is the moment of inertia, $\beta_*^2 = GM/Rc^2$, and all values have been scaled to those appropriate for our CO6 model (Tables 1 & 2).

Equation (17) is a central result of this paper. It is independent of eigenmode properties and is only weakly dependent on the orbital period, although it depends strongly on the mass, radius, and companion mass. Eigenmode properties do of course dictate when this value of $\mathcal{Q}_\mathrm{t}$ is applicable, i.e., when resonance locks are able to occur. We will further show in § 7.2 that equation (17) can hold even when the dynamical tide is a traveling wave, and the standing wave formalism presented thus far is invalid.

Values of the various quantities entering into equation (17) are provided for a selection of helium and carbon/oxygen WD models in Table 1. In particular, since the inspiral time is much longer for low-mass helium WDs than for more massive carbon/oxygen WDs, equation (17) predicts that the tidal quality factor $\mathcal{Q}_\mathrm{t}$ should be much larger ($\sim 100\times$) for helium WDs, as shown in Table 2, meaning tidal effects are more efficient in carbon/oxygen WDs.

5.2 Tidal heating

The rate at which heat is dissipated in the WD assuming solid-body rotation can be derived using equation (B8):

$$\begin{aligned}\dot{E}_\mathrm{heat} &= \dot{E}_\mathrm{tide} - \dot{E}_\mathrm{mech} \\ &= \Omega\tau - \frac{d}{dt}\left(\frac{1}{2} I_* \Omega_\mathrm{spin}^2\right) \\ &= I_* \dot{\Omega}_\mathrm{spin} \delta\Omega = \frac{E_\mathrm{tide}\, \delta\Omega}{\mathcal{Q}_\mathrm{t}},\end{aligned} \tag{18}$$

where $\delta\Omega = \Omega - \Omega_\mathrm{spin}$. During a resonance lock we have $\dot{\Omega}_\mathrm{spin} \approx \dot{\Omega} = \Omega/t_\mathrm{gw}$, so that

$$\dot{E}_\mathrm{heat} \approx \frac{I_* \Omega\, \delta\Omega}{t_\mathrm{gw}}, \tag{19}$$

with $\delta\Omega$ then being approximately constant (having neglected rotational modification of WD eigenmodes; see § 9.2). Defining the asynchronicity period as $\delta P = 2\pi/\delta\Omega$, we can evaluate this further as

$$\begin{aligned}\dot{E}_\mathrm{heat} \approx 1.4 \times 10^{-2}\, L_\odot &\left(\frac{M'}{M}\right) \left(\frac{1+M'/M}{2}\right)^{-1/3} \\ &\times \left(\frac{P_\mathrm{orb}}{10\ \mathrm{min}}\right)^{-11/3} \left(\frac{\delta P}{200\ \mathrm{min}}\right)^{-1} \\ &\times \left(\frac{I_*}{0.18 M R^2}\right) \left(\frac{M}{0.6 M_\odot}\right)^{8/3} \left(\frac{R}{0.013 R_\odot}\right)^2,\end{aligned} \tag{20}$$

again scaling variables to our CO6 model's properties (Table 1).

As a simple analytical estimate, consider the example of a resonance lock beginning with the WD unsynchronized at an orbital period P_0 and continuing until the Roche period of $P_\mathrm{Roche} \sim t_* \ll P_0$. The total orbital energy dissipated in the WD as heat in this example is

$$\begin{aligned}\Delta E_\mathrm{heat} &= \frac{2\pi I_*}{P_0} \int \frac{\Omega}{t_\mathrm{gw}} dt \\ &\approx \frac{4\pi^2 I_*}{t_* P_0} \\ &\sim 7.0 E_* \left(\frac{t_*}{P_0}\right) \left(\frac{I_*}{0.18 M R^2}\right),\end{aligned} \tag{21}$$

which could be very large depending on the value of P_0. If for P_0 we use our estimate from § 4 of $P_\mathrm{rl} \sim 170$ min appropriate for our CO6 model, we have $\Delta E_\mathrm{heat} \sim 2 \times 10^{47}$ ergs, a factor of ~ 3 larger than the CO6 model's thermal energy.

Tidal heating can directly add to a WD's luminosity and minimally affect its thermal structure if a) the thermal time $t_\mathrm{th} = pc_p T/gF$ at the outer turning point, where wave damping is most efficient, is smaller than t_gw, and b) $\dot{E}_\mathrm{heat} \ll L$. The outer turning point occurs due to the outer convection zone, so $t_\mathrm{th}|_\mathrm{rcb}$ (radiative-convective boundary) is an appropriate value to use. We find $t_\mathrm{th}|_\mathrm{rcb} \lesssim 10^6$ years for all of our WD models, as shown in Table 1; this is $\ll t_\mathrm{gw}$ for $P_\mathrm{orb} \gtrsim 10$ min, implying that criterion (a) is satisfied. Moreover, for all models other than our $T_\mathrm{eff} = 5,100$ K helium and $T_\mathrm{eff} = 5,500$ K carbon/oxygen WDs, $t_\mathrm{th}|_\mathrm{rcb} \lesssim 50$ years, and $t_\mathrm{th}|_\mathrm{rcb} \lesssim t_\mathrm{gw}$ is satisfied even directly prior to mass transfer.

Criterion (b) above is more restrictive: examining equation (20) shows that near orbital periods of ~ 10 min, the tidal heating rate approaches typical WD luminosities. The orbital period where this occurs depends weakly on the various parameters appearing in equation (20), since $\dot{E}_\mathrm{heat} \propto P_\mathrm{orb}^{-11/3}$. Thus the thermal

structure of WDs in close binaries may adjust significantly to accommodate the additional heat input for $P_{\rm orb} \lesssim 10$ min. We discuss the consequences of tidal heating further in § 9.2.

5.3 Tidally enhanced orbital decay

Although the rate $\dot{P}_{\rm orb}$ at which the orbital period of an inspiraling WD binary decays is dominated by the gravitational wave term $\dot{P}_{\rm gw} = -P_{\rm orb}/t_{\rm gw}$, tidal energy dissipation implies a small deviation from this value (see also Piro 2011).[2] We can compute this difference for a system consisting of two WDs both undergoing resonance locks by using equations (6), (7), and (B8), which yield

$$\dot{P}_{\rm orb} = \dot{P}_{\rm gw} + \dot{P}_{\rm tide}, \tag{22}$$

where

$$\dot{P}_{\rm tide} = \left(\frac{S}{1-S}\right)\dot{P}_{\rm gw}, \quad S \approx 3\left(\frac{I_1+I_2}{\mu a^2}\right), \tag{23}$$

$I_{1,2}$ are the moments of inertia of the two WDs, $\mu = M_1M_2/(M_1 + M_2)$ is the reduced mass, a is the semi-major axis, and we have again neglected rotational modification of WD eigenmodes (i.e. $\partial\omega_n/\partial\Omega_{\rm spin} = 0$, where ω_n is a corotating-frame eigenfrequency; see § 9.2). This effect may be detectable in future observations of close WD binaries, as discussed in § 9.1.

6 APPLICABILITY OF STANDING WAVES

6.1 Wave breaking

It is important to determine whether the dynamical tide we are attempting to study represents a standing wave or a traveling wave. If it is a standing wave, meaning it is able to reflect at its inner and outer turning points without being absorbed, then it can achieve large amplitudes due to resonances with tidal forcing frequencies (as assumed in § 4). In the absence of nonlinear effects that can occur at large amplitudes, a standing wave's damping rate is well approximated by the quasiadiabatic value (Appendix B3), which is small for WDs due to their high densities and long thermal times (see Figure B1). On the other hand, if the dynamical tide instead behaves as a traveling wave, resulting from absorption prior to reflection, then its damping time is approximately a group travel time.

In this section we determine whether the nonlinear process of gravity wave breaking causes tidally excited g-modes in WDs to be absorbed near the surface and hence to become traveling waves, as has been suggested in recent studies (Fuller & Lai 2011, 2012). Gravity wave breaking has been considered extensively in the atmospheric science community, since it occurs in Earth's atmosphere; see e.g. Lindzen (1981). It is also thought to occur in the cores of solar-type stars (Goodman & Dickson 1998; Barker & Ogilvie 2010).

Breaking occurs when a wave's amplitude becomes large enough to disrupt the stable background stratification. One way to derive the condition under which this happens is to determine when a wave would produce its own convective instability, which is equivalent to the perturbed Brunt-Väisälä frequency (squared) becoming comparable to the background value—this then makes the total value negative, implying convection. The Eulerian perturbation to N^2 is given in linear theory by

$$\frac{\delta N^2}{N^2} \approx k_r\xi_r - \frac{\delta p}{p} - \frac{\xi_r}{H_\rho} + \frac{\delta g}{g}, \tag{24}$$

where H_ρ is the density scale height and k_r is the wavenumber in the direction of gravity. Since $k_r\xi_r$ is much larger in magnitude than the other terms for g-modes, the wave breaking condition thus becomes

$$|k_r\xi_r| \sim 1. \tag{25}$$

Other nonlinear processes also come into play when $|k_r\xi_r| \sim 1$. Indeed, this criterion is equivalent to Ri $\sim 1/4$, where Ri is the Richardson number due to the wave's shear, which implies the wave is Kelvin-Helmholtz unstable. Equation (25) is also similar to the condition under which surface ocean waves break: when the vertical displacement becomes comparable to the wavelength.

To determine whether g-modes break, we evaluated the linear, quadrupolar tidal fluid response assuming global adiabatic normal modes and an equal-mass companion; see Appendix B. Under these assumptions, we find that for both our helium and carbon/oxygen WD models, the dynamical tide breaks for close resonances at orbital periods as large as ~ 1 hr, as shown in Figure 3. The off-resonance dynamical tide begins to break more generically at $P_{\rm orb} \lesssim 10 - 20$ min.[3] Furthermore, for all of the WD models we have considered (Table 1), we find that at sufficiently long orbital periods, the dynamical tide doesn't break even for a perfect resonance, and thus that standing wave resonance locks should be able to occur. As such, we expect wave breaking not to operate during a significant portion of the inspiral epoch, in which case the analysis presented in § 4 may be valid. We address this in more detail in § 8.

6.2 Differential rotation and critical layers

The possibility of differential rotation represents a significant challenge to the standing wave assumption we utilized in § 4. Indeed, tidal angular momentum is preferentially deposited in the outer layers of a WD, since that is where damping times are shortest and waves are able to communicate their energy and angular momentum content to the background stellar profile (Goldreich & Nicholson 1989b). Thus tides do not naturally induce solid-body rotation, and instead tend to first synchronize layers near the outer part of the gravity wave propagation cavity (Goldreich & Nicholson 1989a), absent the influence of efficient internal angular momentum transport.

The presence of a synchronized or "critical" layer at the edge of a mode propagation cavity implies that the mode's corotating frequency tends to zero at that location, which in turn means its radial wavenumber becomes very large due to the asymptotic g-mode dispersion relation $\omega \sim N(k_{\rm h}/k_r)$, where $k_{\rm h}$ and k_r are respectively the perpendicular and radial wavenumbers. As a result, the mode's local damping time becomes very short, and it is absorbed rather

[2] Note that the purpose of this section is to determine the influence of the tidal energy deposition term $\dot{E}_{\rm tide}$ on the rate of orbital decay, even though this term is neglected everywhere else in this work, as justified in § 4.

[3] This is in conflict with the claims made in Fuller & Lai (2012), since that work used $k_r|\boldsymbol{\xi}| \sim 1$ to assess wave breaking, instead of equation (25). The total displacement $|\boldsymbol{\xi}| = (\xi_r^2 + \xi_{\rm h}^2)^{1/2}$ includes horizontal motion, which is perpendicular to the stratification and thus does not contribute to breaking. As a g-mode's horizontal motion is much greater than its vertical motion, Fuller & Lai (2012) overestimated the degree of breaking by a factor of $\sim \xi_{\rm h}/\xi_r \sim \omega_*/\sigma \gg 1$, where $\sigma = 2(\Omega - \Omega_{\rm spin})$ is the $l = m = 2$ tidal driving frequency.

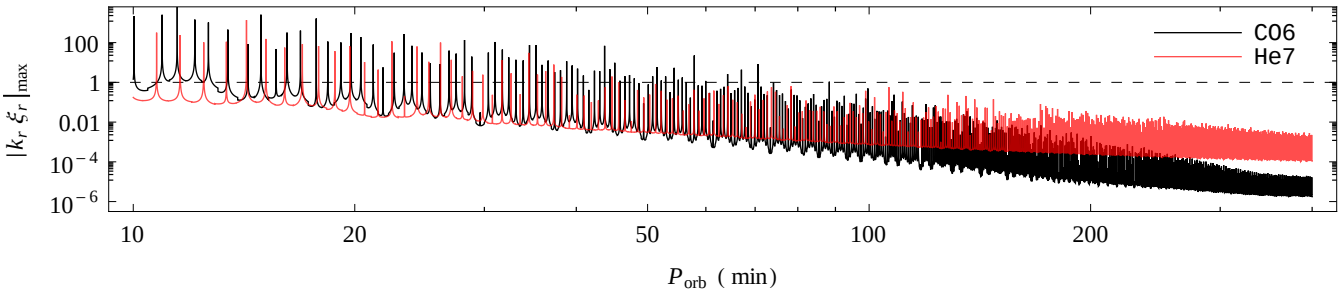

Figure 3. The maximum value of $|k_r\xi_r|$ attained throughout the propagation cavity of our CO6 (black line) and He7 (red line) WD models (Table 1), assuming adiabatic standing waves, $\Omega_{\rm spin} = \Omega/2$, and an equal-mass companion. Where $|k_r\xi_r|_{\max} > 1$, wave breaking occurs (§ 6.1), and the effective wave damping time becomes roughly the group travel time across the WD. This occurs very near resonances for $P_{\rm orb} \lesssim 0.5$ – 1 hr.

than reflected, eliminating the possibility of achieving resonant amplitudes (although traveling waves can also effect resonance locks at short orbital periods; § 7).

In Appendix A we analyze angular momentum redistribution by fossil magnetic fields, possibly generated by a progenitor star's convective core (during hydrogen or helium fusion) and amplified by flux freezing as the core contracts. We calculate that a field strength of only ~ 200 G is required to maintain solid-body rotation during a resonance lock for an orbital period of ~ 100 min in our CO6 model, and only ~ 20 G in our He7 model (Table 1). Liebert et al. (2003) conclude that at least $\sim 10\%$ of WDs have fields $\gtrsim 10^6$ G, and speculate that this fraction could be substantially higher; field strengths in WD interiors may be even more significant. With a field of 10^6 G, our calculations indicate that critical layers should not occur until orbital periods of less than 1 min, or even less if the field can wind up significantly without becoming unstable.

6.3 Validity of the secular approximation

The Lorentzian mode amplitude solutions invoked in Appendix B to produce the standing wave torque in equation (4) are strictly valid only when a mode's amplitude changes slowly relative to its damping time. Further examining equation (5), we see that near a perfect resonance the amplitude changes by a factor of ~ 2 as the detuning frequency changes by of order the damping rate γ_n. Thus the Lorentzian solution is applicable near a perfect resonance only when

$$\gamma_n^{-1} \lesssim t_{\rm gw} \frac{\gamma_n}{\Omega}, \tag{26}$$

which evaluates to

$$P_{\rm orb} \gtrsim 90 \text{ min} \left(\frac{M}{0.6 M_\odot}\right)^{5/11} F_{\rm sec}, \tag{27}$$

where

$$F_{\rm sec} = \left(\frac{M'}{M}\right)^{3/11} \left(\frac{1+M'/M}{2}\right)^{-1/11} \left(\frac{\gamma_n^{-1}}{80 \text{ yr}}\right)^{6/11}.$$

Equation (27) is scaled to values for our CO6 model (Figure 6); the restriction instead evaluates to $P_{\rm orb} \gtrsim 50$ min for our He7 model, using a damping time of $\gamma_n^{-1} \sim 60$ yr appropriate for the initial resonance lock. Below these periods, the Lorentzian solution becomes invalid and the exact outcome is unclear, although our preliminary numerical integrations of fully coupled mode amplitude and orbital evolution equations indicate that resonance locks can still occur even beyond the validity of the Lorentzian solution. (We address a similar concern relating to angular momentum transport in Appendix A2.) Nonetheless, we find that the initial standing wave resonance lock occurs at orbital periods larger than the critical value from equation (27) in our CO6 and He7 models (Table 2), meaning resonance locks should proceed as expected.

7 TRAVELING WAVES

7.1 Excitation and interference

In this section, we will describe two different mechanisms of tidal gravity wave excitation considered in the literature. We will then compare both sets of theoretical predictions to our numerical results to assess which mechanism predominantly operates in our fiducial WD models.

Zahn (1975) showed that when a gravity wave is well described by its WKB solution, a conserved wave energy flux results. Thus gravity waves must be excited where the WKB approximation is invalid: where the background stellar model—particularly the Brunt-Väisälä frequency N—changes rapidly relative to a wavelength.

One natural candidate for wave excitation, then, is at a radiative-convective boundary (RCB), where N^2 abruptly becomes negative. WDs possess convective envelopes near their surfaces (Figure 1), so this mechanism is plausible. The resulting theoretical prediction (Zahn 1975; Goodman & Dickson 1998) is that the traveling wave tidal torque should scale as $\tau \propto \sigma^{8/3}$, where $\sigma = 2(\Omega - \Omega_{\rm spin})$ is the $m = 2$ tidal driving frequency. Using our calculation of the traveling wave torque in equation (32) from § 7.2, we see that this in turn implies that the linear overlap integral (Appendix B4) should scale as $Q_n \propto \omega_n^{11/6}$, given our normalization convention in equation (B5).

More recently, Fuller & Lai (2012) showed that excitation can also proceed near the spike in the Brunt-Väisälä frequency that occurs at the transition between carbon/oxygen and helium in a carbon/oxygen WD (see Figure 1). Their corresponding prediction for the torque scaling is $\tau \propto \sigma^5$, implying $Q_n \propto \omega_n^3$. Thus this mechanism predicts a steeper overlap scaling with frequency than for excitation at the RCB.

An additional feature of excitation at a composition boundary is that waves originate from a location inside the propagation cavity, meaning both an ingoing and outgoing wave are created. Since the ingoing wave reflects at the inner turning point, interference occurs between the reflected ingoing wave and the purely outgo-

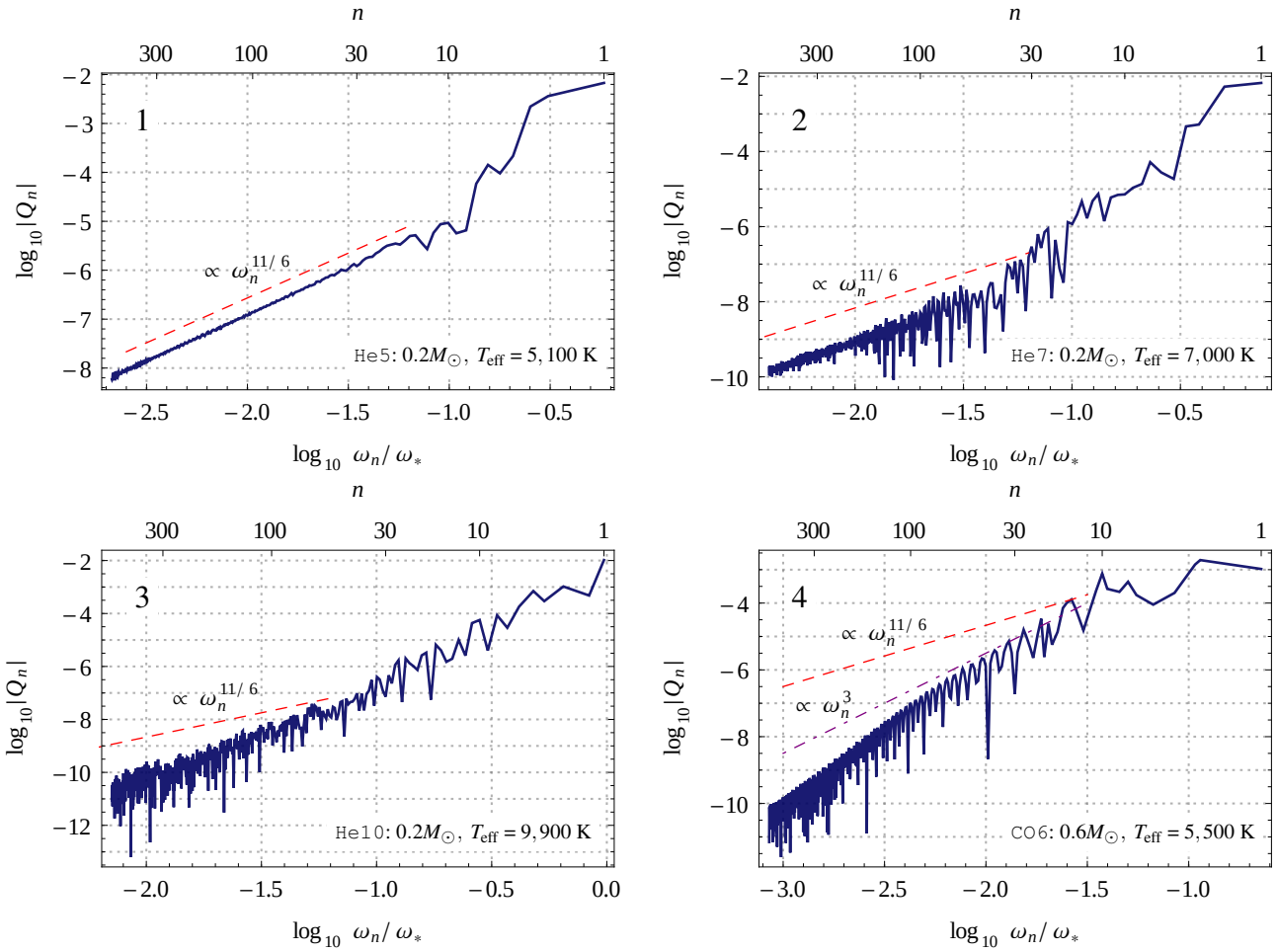

Figure 4. Plots of the linear tidal overlap integral Q_n, which characterizes the spatial coupling strength between the tidal potential and a given mode (Appendix B4), as a function of the eigenmode frequency ω_n and radial order n, for the first 500 g-modes in four of our fiducial WD models (Table 1). Panels 1 – 3 are helium WDs ordered by increasing temperature; panel 4 is a carbon/oxygen WD. A smooth power law scaling of $Q_n \propto \omega_n^{11/6}$ implies that gravity wave excitation by the tidal potential occurs at the interface between a WD's outer convection zone and its inner radiative core (§ 7.1); this can be seen in the cooler helium models from panels 1 & 2. Hotter WDs have smaller convective regions, and wave excitation instead may occur at composition gradient zones (Fuller & Lai 2012); this mechanism predicts steeper, more jagged profiles of Q_n with ω_n, as in panels 3 & 4.

ing wave. Constructive interference implies a large overlap integral Q_n, whereas destructive interference makes the overlap small, thus this mechanism predicts a jagged overlap profile with respect to the wave frequency ω_n.

With these theoretical predictions in hand, the essential question to answer is which excitation mechanism—RCB or composition gradient—is most efficient in a given WD model.[4] The answer hinges on the properties of the convective envelope. Table 1 and Figure 1 show that this envelope is very small in hot WDs, and exists at very low densities, but that its extent increases rapidly as a WD cools. Thus it seems possible that excitation at the RCB may occur for cooler WDs, whereas hotter WDs must rely on the composition gradient mechanism.

One method we can utilize to distinguish between the two mechanisms is simply to observe the power law scaling $Q_n \propto \omega_n^a$ of numerically computed linear overlap integrals for our various WD models, given in Table 3. Consistent with our expectations, cooler helium WDs have a power law index $a \sim 1.83 \approx 11/6$, implying excitation at the RCB, while hotter helium WDs and our carbon/oxygen models have larger values of a. Furthermore, Figure 4 shows that models with steeper overlap power laws also show jagged variation of Q_n with frequency, thus demonstrating the interference predicted by composition gradient excitation.

Note that if a gravity wave in a cool helium WD begins to break near its outer turning point (§ 6.1), this implies that the tidal excitation and wave breaking regions would be almost directly adjacent. It might then be possible for breaking to inhibit excitation, meaning that the composition gradient mechanism would again dominate. A more sophisticated hydrodynamical calculation is required to address this concern.

7.2 Traveling wave resonance locks

The resonance lock scenario we described in § 4 relied on resonances between standing WD eigenmodes and the tidal driving frequency. However, resonance locks are in fact a more general phe-

[4] This question was not addressed in Fuller & Lai (2012) since they adopted an absorbing boundary condition near the outer turning point, and thus did not include the convection zone in their calculations.

Table 3. WD $l = 2$ eigenmode properties. Asymptotic fits to numerically computed eigenmode properties for the WD models from Table 1. The linear overlap integral Q_n (Appendix B4 & Figure 4) is fit as $Q_n = Q_0(\omega_n/\omega_*)^a$; the damping rate γ_n (Appendix B3 & Figure B1) is fit as $\gamma_n = \gamma_0(\omega_n/\omega_*)^{-b}$; and the inverse group travel time $\alpha_n = 2\pi/t_{\mathrm{group},n}$ (Appendix B3) is fit as $\alpha_n = \alpha_0(\omega_n/\omega_*)^c$. †Note that rapid thermal diffusion near the outer turning point causes g-modes of radial order $n \gtrsim 50$ to become traveling waves in our `CO12` and `He10` models, meaning our fits for γ_n are not relevant in this regime; see Appendix B3 and Figure B1.

ID	Q_0	a	γ_0/ω_*	b	α_0/ω_*	c
`He10`†	9.6×10^{-6}	2.61	1.5×10^{-11}	6.16	0.0891	2.00
`He7`	3.6×10^{-6}	1.83	2.1×10^{-12}	2.00	0.158	2.00
`He5`	7.8×10^{-4}	1.90	7.7×10^{-15}	1.99	0.298	2.00
`CO12`†	7.2×10^{1}	4.40	1.2×10^{-14}	6.41	0.403	2.00
`CO6`	2.7×10^{1}	3.69	2.9×10^{-14}	1.88	0.743	2.00

nomenon that does not explicitly require standing waves.[5] In the context of WD binary inspiral, the two essential requirements on the tidal torque function τ in order for a resonance lock to occur are:

a) The torque profile must be a jagged function of the $l = m = 2$ tidal driving frequency $\sigma = 2(\Omega - \Omega_{\mathrm{spin}})$ (equation 31 below).

b) The magnitude of the tidal torque must be large enough that it can satisfy equation (9): $\tau = I_*\Omega/t_{\mathrm{gw}}$.

When these conditions are satisfied and a resonance lock occurs, the tidal quality factor $\mathcal{Q}_{\mathrm{t}}$ and heating rate are given by equations (17) and (20), respectively.

We first address criterion (a). Dropping the tidal energy deposition term from equation (7), as justified in § 4, yields the simplified orbital evolution equation

$$\frac{1}{m}\frac{d\sigma}{d\Omega} = 1 - \frac{t_{\mathrm{gw}}\tau}{I_*\Omega}, \tag{28}$$

where the gravitational wave decay time $t_{\mathrm{gw}}(\Omega)$ is defined in equation (1).

Let us assume that the tidal torque satisfies criterion (b) at an orbital frequency Ω_0 and a tidal driving frequency σ_0, so that $d\sigma/d\Omega = 0$ and equation (28) reduces to

$$I_*\Omega_0 = t_{\mathrm{gw}}(\Omega_0)\tau(\Omega_0, \sigma_0). \tag{29}$$

As long as τ increases with σ, equation (29) represents a stable fixed point of the evolution equations; see Figure 2. Next, since the orbital frequency steadily increases due to the emission of gravitational waves, we examine what happens to this fixed point when Ω changes by a small amount $+\Delta\Omega$. In order to preserve equation (29), the tidal driving frequency must commensurately change by an amount $\Delta\sigma$ given by

$$\frac{\Delta\sigma}{\sigma} = -\frac{1}{3}\left(\frac{\Delta\Omega}{\Omega}\right)\left(\frac{\partial\log\tau}{\partial\log\sigma}\right)^{-1}, \tag{30}$$

which can be derived by differentiating equation (29) and substituting equation (1).

Equation (30) allows us to appropriately quantify the "jagged" variation of the torque function required by criterion (a): if

$$\left|\frac{\partial\log\tau}{\partial\log\sigma}\right| \gg 1, \tag{31}$$

then the fixed point can be maintained by only a minimal change in the forcing frequency for a given increase in the orbital frequency, thus constituting a resonance lock. Any general power law trend of τ with σ will fail to satisfy this condition—additional sharp features are required.[6]

Torque profiles consistent with equation (31) can be provided in several ways. For standing waves, the comb of Lorentzians produced by resonances with eigenmodes (see equation 4 and Figure 3) easily satisfies equation (31), since WD eigenmodes are weakly damped, meaning on- and off-resonance torque values differ by many orders of magnitude. For traveling waves, if the composition gradient mechanism of Fuller & Lai (2012) discussed in § 7.1 is the dominant source of wave excitation, it naturally provides sharp features in the torque function due to wave interference. This can also be observed in Figure 5, where the traveling wave torque changes by a factor of ~ 5 as $\sigma = 2\delta\Omega$ changes by only $\sim 10\%$, implying $|d\log\tau/d\log\sigma| \sim 50$.

Lastly, wave breaking can also provide rapid variation in the torque profile due to a sudden transition between standing and traveling wave torques that occurs near resonances at short orbital periods. Specifically, as the tidal driving frequency σ sweeps towards a resonance due to orbital decay by gravitational waves, a tidally excited g-mode's amplitude can become large enough to induce wave breaking (§ 6.1), which causes the effective damping rate and hence the resulting torque to increase enormously (see the blue curve in Figure 5).

The precise shape of this transition requires hydrodynamical simulations to ascertain. Fortunately, we find that essentially any transition between a nonresonant standing wave torque in between resonances and a traveling wave torque near resonance will satisfy equation (31) for WDs, due to the large disparity between typical damping times associated with standing waves and the group travel time, which approximates the damping time for a traveling wave (Table 3 & Figure B1). We discuss this further in § 8.

Next, we address criterion (b) for a resonance lock stated at the beginning of this section by estimating the magnitude of the traveling wave torque τ_{trav}. Goodman & Dickson (1998) computed τ_{trav} caused by dynamical tides raised in solar-type stars by semi-analytically solving for the traveling wave tidal response.[7] Then, to approximate the effect of discrete resonances, they attached Lorentzian profiles to their formula for τ_{trav}. We reverse this procedure, and instead approximate τ_{trav} by our standing wave formula in the limit that the mode damping time approaches the group travel time. We establish the fidelity of this approximation in Appendix C.

We thus compute τ_{trav} by first using equation (5) with the tidal driving frequency σ set to a particular eigenfrequency ω_n, γ_n re-

[5] In the traveling wave regime, true "resonances" do not occur. Nonetheless, we continue using the term "resonance lock" in this context due to the many similarities between standing wave and traveling wave results. In particular, the tidal evolution scenario associated with what we call a traveling wave resonance lock is identical to that associated with a true resonance lock in the standing wave regime, and the transition between standing and traveling wave torques introduced by wave breaking occurs near would-be standing wave resonances.

[6] Fuller & Lai (2012) also noticed that $\sigma \approx$ constant occurred in their simulations, although they attributed this to the overall power law trend of their torque function with σ. Indeed, their results possess sharp interference-generated features that provide a much larger contribution to $|d\log\tau/d\log\sigma|$ than the trend, meaning a resonance lock was likely responsible for maintaining $\sigma \approx$ constant.

[7] Goodman & Dickson (1998) explicitly computed the tidal energy deposition rate $\dot{E}_{\mathrm{tide}}$; this can be converted to a torque using equation (B8).

placed by $\alpha_n = 2\pi/t_{\rm group,n}$ (where $t_{\rm group}$ is the group travel time; see Appendix B3), and $\delta\omega_n$ set to zero. This yields

$$\tau_{\rm trav}(\sigma=\omega_n,\Omega) \sim 4E_*\varepsilon^2 Q_n^2\omega_n/\alpha_n, \tag{32}$$

where we have approximated $W^2 \approx 1$. Then, in order to evaluate an effective traveling wave torque for arbitrary σ, we simply interpolate over values computed using equation (32).

To estimate the first orbital period $P_{\rm trl}$ at which traveling wave resonance locks can occur, we follow the same procedure as in § 4 and again invoke approximate scalings for the eigenmode linear tidal overlap integral Q (Appendix B4) and the effective traveling wave damping rate α (Appendix B3):

$$Q \approx Q_0(\sigma/\omega_*)^a \quad \text{and} \quad \alpha \approx \alpha_0(\sigma/\omega_*)^c,$$

where $c = 2$; see Table 3 and Figure B1. The resulting formula, scaled to values for our CO6 model (Table 1), is

$$P_{\rm trl} \sim 43\ {\rm min}\left(\frac{t_*}{2.9\ {\rm s}}\right) F_{\rm trl}^q, \tag{33}$$

where $t_* = (R^3/GM)^{1/2}$ is the WD's dynamical time, the factor $F_{\rm trl}$ is

$$\begin{aligned} F_{\rm trl} \sim & \left(\frac{M'}{M}\right)\left(\frac{1+M'/M}{2}\right)^{-5/3} \\ & \times \left(\frac{\beta_*}{0.010}\right)^{-5}\left(\frac{I_*}{0.18MR^2}\right)^{-1} \\ & \times \left(\frac{Q_0}{27}\right)^2\left(\frac{\alpha_0}{0.74\omega_*}\right)^{-1} \\ & \times \left(8.41\times10^{12}\right)(0.0119)^{1/q}, \end{aligned} \tag{34}$$

the power q is in general

$$q = \frac{1}{-1/3+2a} < 1, \tag{35}$$

and $q = 0.15$ for our CO6 model (Table 3). (The last line of equation 34 is equal to unity for $q = 0.15$.) Equation (33) assumes the WD begins completely unsynchronized; it is equivalent to equation (79) of Fuller & Lai (2012).

Direct numerical evaluation of eigenmode properties with our CO6 WD model yields $P_{\rm trl} = 40$ min for an equal-mass companion, due to an $n = 27$ g-mode, which agrees well with equation (33). Values of $P_{\rm trl}$ for each of our fiducial models are provided in Table 2. Note, however, that in deriving these results for $P_{\rm trl}$ we have assumed that the WD spin is much smaller than the orbital frequency; if significant synchronization has already occurred, the true value of $P_{\rm trl}$ will deviate from our prediction by an order-unity factor.

8 NUMERICAL SIMULATIONS

To address the tidal evolution of an inspiraling WD binary undergoing resonance locks, we aim to combine the standing and traveling wave results from §§ 4 & 7 numerically. To this end, we evaluate the complete standing wave tidal torque from equation (4) and solve for the spin and orbital evolution using equation (7). To account for wave breaking, we check that all eigenmodes satisfy $|k_r\xi_r|_{\rm max} < 1$ throughout the WD (§ 6.1); when an eigenmode exceeds unit shear, we instead set its damping rate to $\alpha_n = 2\pi/t_{\rm group,n}$ (Appendix B3), which approximates the traveling wave regime (Goodman & Dickson 1998). We smoothly transition between the standing and traveling wave regimes using the interpolation formula

$$\tau = \frac{\tau_{\rm stand} + \tau_{\rm trav}\left(|k_r\xi_r|_{\rm max}\right)^z}{1+\left(|k_r\xi_r|_{\rm max}\right)^z}, \tag{36}$$

where $\tau_{\rm stand}$ is the standing wave torque from equation (4), $\tau_{\rm trav}$ is the traveling wave torque produced by interpolating over equation (32), and $|k_r\xi_r|_{\rm max}$ is the maximum value of the wave shear over all relevant eigenmodes and across the entire propagation cavity (§ 6.1), evaluated assuming standing waves. We arbitrarily adopt $z = 25$ to induce a sharp transition that occurs only when $|k_r\xi_r|_{\rm max}$ is very close to 1; our results are insensitive to the value of z so long as it is $\gtrsim |\ln(\tau_{\rm trav}/\tau_{\rm stand})|$. Figure 5 shows a comparison of $\tau_{\rm stand}$, $\tau_{\rm trav}$, and the transition function in equation (36).

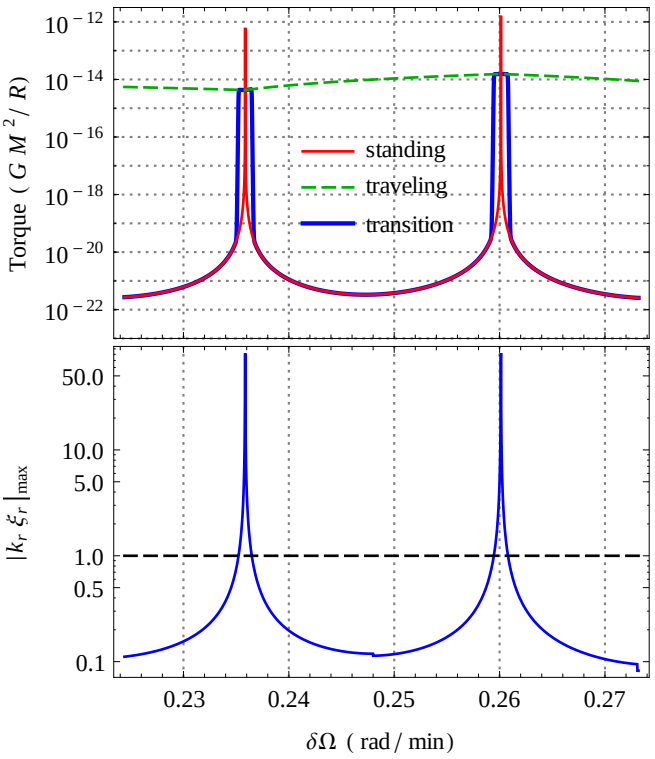

Figure 5. *Top panel:* Example plot of the standing wave torque $\tau_{\rm stand}$ (equation 4; red line), the traveling wave torque $\tau_{\rm trav}$ (interpolation over equation 32 evaluated at eigenmode frequencies; dashed green line), and our interpolation between the two regimes (equation 36; thick blue line), as functions of $\delta\Omega = \Omega - \Omega_{\rm spin}$ at fixed $P_{\rm orb} = 30$ min for our CO6 model (Table 1) and an equal-mass companion. The standing wave torque on average is many orders of magnitude smaller than the traveling wave torque; however, near resonances it becomes many orders of magnitude larger. Wave breaking acts to "cap" the Lorentzian peaks of the standing wave torque in the interpolation function. *Bottom panel:* Plot of the wave breaking criterion $|k_r\xi_r|$ maximized over all eigenmodes and the entire propagation cavity (blue line), using the same parameters and model as the top panel. When $|k_r\xi_r|_{\rm max} < 1$, the dynamical tide represents a traveling wave, and the torque $\tau \to \tau_{\rm stand}$; when $|k_r\xi_r|_{\rm max} > 1$, wave breaking occurs, and $\tau \to \tau_{\rm trav}$ (§ 6.1).

Figure 6 shows the results of two of our simulations. The left column used our $0.2M_\odot$, $T_{\rm eff} = 7{,}000$ K He7 model, while the right column used our $0.6M_\odot$, $T_{\rm eff} = 5{,}500$ K CO6 model (Table 1). We did not account for WD cooling or tidal heating, and instead used fixed WD models throughout both simulations. We initialized our simulations with $\Omega_{\rm spin} \sim 0$, and the orbital period set so that the

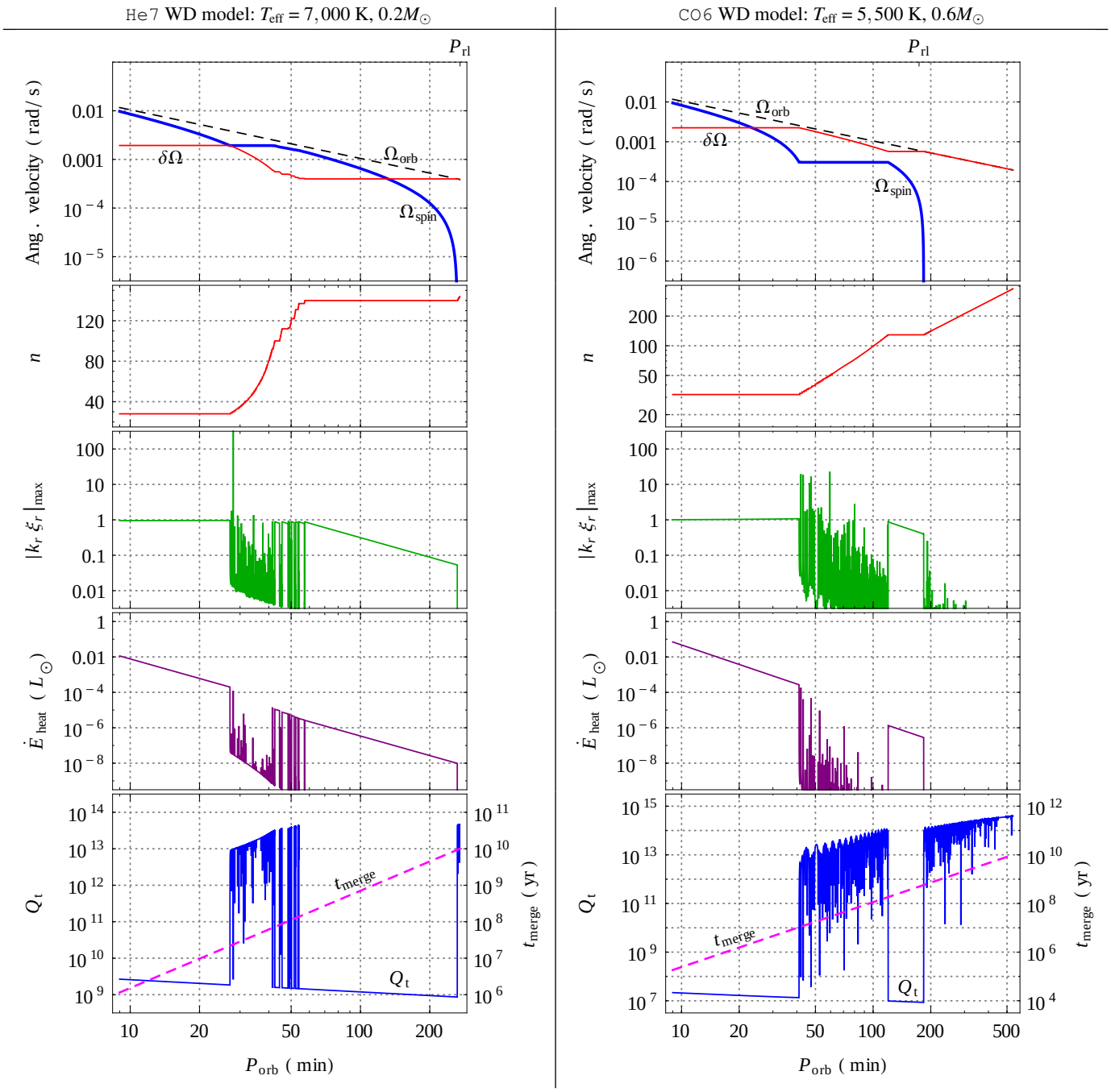

Figure 6. Results of numerical simulations of the secular evolution of WD binaries, the details of which are described in § 8. The left column shows results using our $0.2M_\odot$, $T_{\rm eff} = 7,000$ K He7 model, while the right column used our $0.6M_\odot$, $T_{\rm eff} = 5,500$ K CO6 model (Table 1). *Top row:* The orbital (dashed black line) and spin (thick blue line) frequencies, as well as their difference $\delta\Omega = \Omega - \Omega_{\rm spin}$ (red line); the latter sets the tidal forcing frequency $\sigma = 2\delta\Omega$. Resonance locks correspond to regions where $\delta\Omega$ is constant. Our assumption of slow rotation breaks down when $\delta\Omega \lesssim \Omega_{\rm spin}$ due to nonlinear rotational modification of stellar eigenmodes. *Second row:* Number of radial nodes n of dominant eigenmode/wave. *Third row:* Maximum value of $|k_r\xi_r|$ across entire WD, evaluated assuming standing waves, which assesses whether wave breaking occurs (§ 6.1). During the initial resonance lock, $|k_r\xi_r|_{\rm max}$ starts < 1, but gradually rises until it becomes ~ 1 and breaking begins. *Fourth row:* Rate at which orbital energy is dissipated as heat in the WD, in units of $L_\odot$. *Bottom row:* Tidal quality factor $\mathcal{Q}_{\rm t}$ (blue line) and time until mass transfer $t_{\rm merge} = 3t_{\rm gw}/8$ (equation 1; dashed magenta line). See equations (17) and (20) for analytic estimates of the tidal quality factor $\mathcal{Q}_{\rm t}$ and heating rate, respectively.

time until mass transfer $t_{\rm merge} = 3t_{\rm gw}/8$ (equation 1) was equal to 10 billion years.

Both simulations follow the archetypal scenario laid out in § 3, transitioning amongst the four regimes (S1), (S2), (T1), and (T2). Both begin in (S1), where the dynamical tide is a standing wave even near resonances, but the tidal torque is too weak to create a resonance lock. As the orbit shrinks due to gravitational wave radiation, the tidal force waxes and the first resonance lock eventually begins in both simulations at the appropriate value of $P_{\rm rl}$ estimated in § 4 and provided in Table 2; this is regime (S2). At this point tidal

heating and synchronization suddenly become much more efficient (§ 5), and the difference between orbital and spin frequencies remains constant. Analytic formulas for the tidal quality factor and heating rate appropriate for this situation (as well as T2 discussed below) are given in equations (17) and (20), respectively, and exactly reproduce their numerically derived values appearing in the bottom two rows of Figure 6.

Both simulations begin the standing wave resonance lock regime (S2) with a value of the wave breaking criterion $|k_r\xi_r|_{\max} < 1$; however, as the orbit shrinks further, progressively larger and larger wave amplitudes become necessary to support a resonance lock, eventually leading to wave breaking near the outer turning point (§ 6.1). At the onset of (S2) in the `CO6` simulation, the inequality $|k_r\xi_r|_{\max} < 1$ is only weakly satisfied, meaning that the standing wave lock regime (S2) is short lived. In the `He7` simulation, however, (S2) begins with $|k_r\xi_r|_{\max} \ll 1$, so that the initial resonance lock persists from $P_{\rm rl} = 270$ min to a period of $P \approx 50$ min, corresponding to an interval of time of about 5 billion years.

Once $|k_r\xi_r|_{\max}$ becomes ~ 1, both simulations enter regime (T1), where near would-be resonances the dynamical tide becomes a traveling wave too weak to create a resonance lock. The otherwise steeply peaked standing wave torque is thus capped in this regime; see Figure 5. Regime (T1) results in a weak tidal synchronization and heating scenario, very similar to (S1).

Eventually, at an orbital period $\sim P_{\rm trl}$ (§ 7.2; Table 2), both simulations enter regime (T2), where even the traveling wave torque can create a resonance lock (terminology discussed further in footnote 5). Tides again become efficient, with synchronization and heating scenarios quantitatively consistent with the analytic results in § 5 (just as in S2). In the `He7` simulation, (T2) begins at an orbital period of ≈ 27 min, which differs from its value of $P_{\rm trl} = 49$ min listed in Table 2, since that value is only strictly applicable when $\Omega_{\rm spin} = 0$, whereas significant synchronization has already occurred. The value of $P_{\rm trl}$ in the `CO6` simulation is a better estimate of the onset of (T2) due to the brief duration of (S2) in that case.

The maximum wave shear $|k_r\xi_r|_{\max}$ shown in Figure 6 (which is evaluated assuming standing waves) remains very close to unity throughout much of regime (T2). A reasonable question, then, is whether this is an artifact of the interpolation function we used to transition between standing and traveling waves torques (equation 36).

On the contrary, we believe there is a physical reason why $|k_r\xi_r|_{\max}$ should saturate at ~ 1, and that it is a natural consequence of the traveling wave resonance lock scenario we proposed in § 7.2. Specifically, at this point in the system's evolution, if the dynamical tide attempts to set up a standing wave, the orbital frequency will evolve, increasing the tidal driving frequency $\sigma = 2(\Omega - \Omega_{\rm spin})$ towards a resonance and inducing wave breaking. However, fully transitioning to the traveling wave regime then creates a much larger torque (due to the much larger effective damping rate), causing the spin frequency to increase rapidly and sending σ away from resonance, ending wave breaking and reinstituting the standing wave regime. The end result is that $|k_r\xi_r|_{\max}$ should average to be ~ 1.

This line of reasoning suggests that the true phenomenon may be episodic in nature. Alternatively, a weak-breaking regime may be possible, allowing the system to smoothly skirt the boundary between linear and nonlinear fluid dynamics. Full hydrodynamical simulations may be necessary to understand this in more detail.

9 DISCUSSION

9.1 Observational constraints

The theoretical results we have developed can be compared to the recently discovered system SDSS J065133.33+284423.3 (henceforth J0651), which consists of a $T_{\rm eff} = 16,500$ K, $0.26 M_\odot$ helium WD in a 13-minute eclipsing binary with a $T_{\rm eff} = 8,700$ K, $0.50 M_\odot$ carbon/oxygen WD (Brown et al. 2011). Orbital decay in this system consistent with the general relativistic prediction was discovered by Hermes et al. (2012).

Piro (2011) studied tidal interactions in J0651, and produced lower limits on values of the tidal quality factor $\mathcal{Q}_{\rm t}$ by assuming that the observed luminosity of each WD is generated entirely by tidal heating, and that both WDs are nonrotating. However, the definition of $\mathcal{Q}_{\rm t}$ used in that work differs with ours (equation 13), which hinders straightforward comparison.[8]

Instead, we compare the observed luminosities with our expression for $\dot{E}_{\rm heat}$ from equation (20), which is applicable during a resonance lock. All parameters for J0651 entering into (20) were determined observationally except the moments of inertia I_* and the asynchronicity periods $\delta P = 2\pi/\delta\Omega$, where $\delta\Omega = \Omega - \Omega_{\rm spin}$. Note that equation (20) counterintuitively shows that greater synchronization leads to diminished tidal heating, since the heating rate is proportional to the degree of synchronization (and hence inversely proportional to δP). We can thus use appropriate values of I_* from Table 1 and impose the inequality $L \gtrsim \dot{E}_{\rm heat}$, since cooling can also contribute to each luminosity, in order to constrain δP for each WD.

This calculation yields $\delta P \gtrsim 7$ min for the helium WD and $\delta P \gtrsim 400$ min for the carbon/oxygen WD, each with uncertainties of $\sim 20\%$. Since the orbital period of J0651 is such that resonance locks should currently exist in both WDs—$P_{\rm orb}$ is less than both $P_{\rm rl}$ from § 4 for standing waves and $P_{\rm trl}$ from § 7.2 for traveling waves (Table 2)—and since our simulations developed wave breaking long before $P_{\rm orb} = 13$ min (Figure 6), our *a priori* expectation is that δP should be $\sim P_{\rm trl} \sim 50$ min for each WD. It is encouraging that the inferred constraints on δP for both WDs are within an order of magnitude of this prediction.

We can nonetheless comment on what the deviations from our predictions may imply. First, the fact that $\delta P > 7$ min $< P_{\rm orb} = 13$ min for the helium WD means that explaining its luminosity purely by tidal heating would require retrograde rotation. Since this situation would be highly inconsistent with our results, we can conclude that its luminosity must be generated primarily by standard WD cooling or residual nuclear burning rather than tidal heating. If this is correct, it would imply an age for the helium WD of only ~ 40 Myr (Panei et al. 2007); dividing this age by a cooling time of ~ 1 Gyr (Table 1) yields a very rough probability for finding such a system of $\sim 4\%$. This scenario does not seem unlikely, however, since selection bias favors younger WDs.

On the other hand, the inferred lower limit of ~ 400 min placed on δP for the carbon/oxygen WD is much larger than our predictions for both $P_{\rm rl}$ and $P_{\rm trl}$. Furthermore, we find that tidal heat is deposited very close to the photosphere in hot carbon/oxygen WD models (Table 1), so we expect tidal heating to contribute directly to the luminosity of the carbon/oxygen WD in J0651 (§ 5.2). The constraint on δP thus means that the carbon/oxygen WD ap-

[8] The relationship between our value of the tidal quality factor, $\mathcal{Q}_{\rm t}$, and that used in Piro (2011), $\mathcal{Q}'_{\rm t}$, is $\mathcal{Q}'_{\rm t} = \mathcal{Q}_{\rm t}\sigma M/\lambda\Omega\mu$, where μ is the reduced mass. Our value $\mathcal{Q}_{\rm t}$ is consistent with being the reciprocal of an effective tidal lag angle, which is the conventional definition; see § 5.1.

pears to be more synchronized than our theoretical expectation, and consequently less luminous than our prediction by a factor of $\sim 400\ \mathrm{min}/P_{\mathrm{trl}} \sim 10$.

Although this is formally inconsistent with our results, examining the first row of Figure 6 shows that both of our numerical simulations have $\delta\Omega \ll \Omega_{\mathrm{spin}}$ near $P_{\mathrm{orb}} = 13$ min. This means that the influence of rotation on eigenmode properties is likely to be very important at such short orbital periods (§ 9.2), which is not included in our analysis. This could lead to enhanced synchronization and hence mollify the discrepancy (since, again, increased synchronization implies less tidal heating). Damping and excitation of WD eigenmodes by nonlinear processes are also likely to be important considerations, which could also increase the efficiency of tidal synchronization.

Lastly, assuming resonance locks are occurring in both WDs, we predict that the rate of orbital decay should be enhanced due to tides by (§ 5.3)

$$\left(\frac{\dot{P}_{\mathrm{tide}}}{\dot{P}_{\mathrm{gw}}}\right)_{\mathrm{J0651}} \sim 3\%,$$

where $\dot{P}_{\mathrm{gw}} = -P_{\mathrm{orb}}/t_{\mathrm{gw}}$. Although this estimate fails to include the effect of rotation on eigenmode frequencies, which we already argued may be important in J0651, it should nonetheless be robust at the order-of-magnitude level. This $\sim 3\%$ deviation between the system's period derivative and the general relativistic prediction not accounting for tides may be detectable given further sustained observations (Piro 2011).

9.2 Rotation and WD evolution

In our analysis we have neglected the influence of rotation on the stellar eigenmodes beyond the simple geometrical Doppler shift of the forcing frequency into the corotating frame. To linear order in the rotation frequency, the correction to the stellar eigenfrequencies makes very little difference to the results we have derived—it just means there should be factors of $(1-C_n) \sim 5/6$ appearing in various formulas in § 4, which we neglected for simplicity.

However, when $\delta\Omega = \Omega - \Omega_{\mathrm{spin}} \lesssim \Omega_{\mathrm{spin}}$, nonlinear rotational effects become important. Figure 6 shows that this inequality is satisfied below $P_{\mathrm{orb}} \sim 25$ min in our `CO6` simulation, and takes hold soon after the first resonance lock in our `He7` simulation, at only $P_{\mathrm{orb}} \sim 150$ min. Below these orbital periods, fully accounting for the Coriolis force in the stellar oscillation equations becomes necessary.

For example, excitation of rotationally supported modes—Rossby waves and inertial waves—could prove very efficient. Such modes have corotating-frame eigenfrequencies that are strongly dependent on the rotation frequency, so a resonance lock would follow the more general trajectory (Witte & Savonije 1999)

$$0 = \dot{\delta\omega} = m\left[\left(1 + \frac{1}{m}\frac{\partial\omega_n}{\partial\Omega_{\mathrm{spin}}}\right)\dot{\Omega}_{\mathrm{spin}} - \dot{\Omega}\right]. \tag{37}$$

Since our analysis in § 5 relied on resonance locks producing $\dot{\Omega} \approx \dot{\Omega}_{\mathrm{spin}}$, which no longer holds when $\partial\omega_n/\partial\Omega_{\mathrm{spin}} \neq 0$, it is unclear whether nonlinear rotational effects could substantially alter our results for e.g. the tidal quality factor (equation 17) and tidal heating rate (equation 20).

WD cooling and tidal heating could also potentially modify the synchronization trajectory that results during a resonance lock. For example, since g-mode frequencies approximately satisfy $\omega_{nl} \sim \langle N\rangle l/n$, and since the Brunt-Väisälä frequency scales with temperature as $N \propto T^{1/2}$ in a degenerate environment (§ 2), progressive changes in a WD's thermal structure due to either heating or cooling would introduce an additional $\partial\omega_n/\partial t$ term on the right-hand side of equation (37).

9.3 Crystallization

Whether a plasma begins to crystallize due to ion-ion electromagnetic interactions is determined by the Coulomb interaction parameter Γ, which is defined as the ratio of the Coulomb to thermal energy,

$$\Gamma = \frac{Z^2 e^2}{d_{\mathrm{i}} kT}, \tag{38}$$

where Ze is the mean ion charge and d_{i} is the ion separation, defined by $1 = n_{\mathrm{i}}(4\pi/3)d_{\mathrm{i}}^3$. When $\Gamma \gtrsim 1$, the plasma under consideration behaves as a liquid; when $\Gamma > \Gamma_{\mathrm{crys}}$, the plasma crystallizes. This critical value is $\Gamma_{\mathrm{crys}} \sim 175$ in single-component plasmas (Dewitt et al. 2001). However, more recent observational studies of carbon/oxygen WD populations (Winget et al. 2009) as well as detailed theoretical simulations (Horowitz et al. 2007) indicate that a larger value of $\Gamma_{\mathrm{crys}} \sim 220$ is applicable for two-component plasmas, as in the cores of carbon/oxygen WDs.

As shown in Table 1, the central value of Γ does not exceed the appropriate value of Γ_{crys} for any of our helium WDs. However, for `CO6`, our $0.6M_{\odot}$, $T_{\mathrm{eff}} = 5{,}500$ K carbon/oxygen WD, we have $\Gamma_{\mathrm{core}} = 260 > \Gamma_{\mathrm{crys}}$, and further $\Gamma > \Gamma_{\mathrm{crys}}$ for 19% of the model by mass (taking $\Gamma_{\mathrm{crys}} = 220$). This is indicated in the bottom panel of Figure 1 as a shaded region.

The excitation of dynamical tides in WDs possessing crystalline cores is an interesting problem that deserves further study. We will only speculate here on the possible physical picture. Our preliminary calculations of wave propagation inside the crystalline core, using expressions for the shear modulus of a Coulomb crystal from Hansen & van Horn (1979), indicate that the shear wave Lamb frequency is several orders of magnitude too large to allow gravity waves to propagate as shear waves in the core.

Thus it seems possible that dynamical tides could be efficiently excited at the edge of the core, as in excitation at the edge of a convective core in early-type stars (Zahn 1975). In this scenario the deviation of the tidal response inside the crystal from the potential-filling equilibrium tide solution excites outward-propagating g-modes. As a consequence, tidal gravity waves may be much more efficiently excited in crystalline core carbon/oxygen WDs, since the Brunt-Väisälä frequency gradient near the core would be much steeper than in any composition gradient zone, as discussed in § 7.1.

9.4 Nonlinear damping

Since eigenmodes responsible for resonance locks in the standing wave regime attain large amplitudes, it is natural to worry that they might be unstable to global nonlinear damping by the parametric instability, even if they don't experience wave breaking (e.g. Arras et al. 2003; Weinberg et al. 2012). To address this, we performed a rough estimate of the threshold amplitude T for the parametric instability to begin sapping energy from the eigenmode responsible for the standing wave resonance lock in our `CO6` simulation from § 8. Using the procedure detailed in § 6.5 of Burkart et al. (2012), we found $T \sim 2 \times 10^{-8}$. On the other hand, during the resonance lock the mode in question began with an amplitude of $|q| \sim 4 \times$

10^{-8}, which grew to $\sim 10^{-7}$ before wave breaking destroyed the lock.

This demonstrates that parametric instabilities may limit the achievable amplitudes of standing waves in close WD binaries, potentially somewhat more stringently than wave breaking alone. Exactly how this affects the overall tidal synchronization scenario requires more detailed study.

10 CONCLUSION

In this paper, we have studied the linear excitation of dynamical tides in WD binaries inspiraling subject to gravitational wave radiation. We showed that the phenomenon of resonance locks occurs generically in this scenario, both when the dynamical tide represents a standing wave or a traveling wave. (Our choice of terminology is discussed further in footnote 5.)

In a resonance lock, as the orbital frequency increases according to $\dot{\Omega} = \Omega/t_{\rm gw}$, where $t_{\rm gw}$ is the gravitational wave inspiral time (equation 1), a synchronizing torque produced by the dynamical tide causes the WD spin frequency to evolve at nearly the same rate: $\dot{\Omega}_{\rm spin} \approx \dot{\Omega}$ (§ 4). This means the $l = m = 2$ tidal driving frequency $\sigma = 2(\Omega - \Omega_{\rm spin})$ remains constant, which in turn keeps the tidal torque nearly constant, leading to a stable situation. In other words, a resonance lock is a dynamical attractor (Figure 2).

We first considered resonance locks created by standing waves, where resonances between the tidal driving frequency and WD eigenmodes create the synchronizing torque required to maintain $\sigma \approx$ constant. We derived analytic estimates of the orbital period $P_{\rm rl}$ at which such resonance locks can first occur (§ 4; also Table 2): $P_{\rm rl} \sim 30$ min for hot carbon/oxygen WDs ($T_{\rm eff} \sim 12,000$ K) and $P_{\rm rl} \sim 200$ min for cold carbon/oxygen WDs ($T_{\rm eff} \sim 6,000$ K). For helium WDs, we found $P_{\rm rl} \sim 70$ min for hot models ($T_{\rm eff} \sim 10,000$ K), and $P_{\rm rl} \sim 1$ day for colder models ($T_{\rm eff} \sim 5,000$ K).

Tides preferentially deposit orbital angular momentum into a WD's outermost layers, where wave damping is most efficient. A concern thus exists that a synchronously rotating critical layer might develop, causing rapid wave damping and eliminating the possibility of maintaining a standing wave (Goldreich & Nicholson 1989b). However, we showed that critical layers are in fact unlikely to develop in the standing wave regime of WD binary inspiral, since a typical WD fossil magnetic field is capable of winding up and enforcing solid-body rotation throughout the WD down to orbital periods of ~ 10 min or less (§ 6.2; Appendix A).

We derived analytic formulas for the tidal quality factor $\mathcal{Q}_{\rm t}$ (equation 17) and heating rate $\dot{E}_{\rm heat}$ (equation 20) during a resonance lock (§ 5). (Since $\mathcal{Q}_{\rm t}$ parametrizes the total tidal energy transfer rate, including mechanical energy associated with changing the WD spin, values of $\mathcal{Q}_{\rm t}$ alone do not determine the tidal heating rate.) Our results predict that, for orbital periods of $\lesssim$ hours, $\mathcal{Q}_{\rm t} \sim 10^7$ for carbon/oxygen WDs and $\mathcal{Q}_{\rm t} \sim 10^9$ for helium WDs. Our formula for $\mathcal{Q}_{\rm t}$ is independent of WD eigenmode properties and weakly dependent on the orbital period, scaling as $\mathcal{Q}_{\rm t} \propto P_{\rm orb}^{-1/3}$. It is, however, strongly dependent on the WD mass and radius. We also found that tidal heating begins to rival typical WD luminosities for $P_{\rm orb} \lesssim 10$ min, a result that is relatively insensitive to WD properties due to the steep power law scaling $\dot{E}_{\rm heat} \propto P_{\rm orb}^{-11/3}$. The analytic results we derived can easily be incorporated into population synthesis models for the evolution of close WD binaries.

As a standing wave resonance lock proceeds, the wave amplitude required to maintain synchronization grows. Eventually, the amplitude becomes so large that the standing wave begins to break near the surface convection zone (§ 6.1). This causes the dynamical tide to become a traveling wave, eliminating the resonance lock. This occurred soon after the initial resonance lock in our $0.6M_\odot$, $T_{\rm eff} = 5,500$ K carbon/oxygen WD simulation; however, the standing wave resonance lock lasted much longer in our $0.2M_\odot$, $T_{\rm eff} = 7,000$ K helium WD simulation, from $P_{\rm orb} \sim 250$ min down to ~ 40 min, amounting to ~ 10 Gyr of binary evolution.

Resonance locks have traditionally been considered only when the dynamical tide represents a standing wave (Witte & Savonije 1999). We showed, however, that given sufficiently short orbital periods, resonance locks can even occur in the traveling wave regime (§ 7.2). We derived two simple criteria for whether traveling waves can effect resonance locks: the traveling wave torque must be large enough to enforce $\dot{\Omega} \approx \dot{\Omega}_{\rm spin}$, and the torque profile as a function of the tidal driving frequency $\sigma = 2(\Omega - \Omega_{\rm spin})$ must possess "jagged" features, a concept quantified by $|d\log\tau/d\log\sigma| \gg 1$ (equation 31), where τ is the tidal torque.

The first criterion is satisfied for orbital periods below a critical period $P_{\rm trl}$, which we found to be $P_{\rm trl} \sim 40 - 50$ min in most WD models (equation 33; Table 2). The second criterion can be satisfied by rapid transitions between standing and traveling wave torques (which differ by orders of magnitude) near resonances as a result of wave breaking (§ 6.1), or by wave interference due to excitation by a composition gradient (§ 7.1; Fuller & Lai 2012). Excitation likely proceeds at a composition gradient in carbon/oxygen WDs and hot helium WDs, but excitation at the radiative-convective boundary becomes important for colder helium WDs with larger surface convection zones (§ 7.1). Excitation off a crystalline core may also be important in cold carbon/oxygen WDs (§ 9.3).

Even after the initial standing wave resonance lock is destroyed by wave breaking, a new traveling wave resonance lock takes hold once the orbital period declines to $P_{\rm orb} \sim P_{\rm trl} \sim 40 - 50$ min. The synchronization trajectory and corresponding values of the tidal quality factor (equation 17) and tidal heating rate (equation 20) are the same during a traveling wave resonance lock. We confirmed our analytic derivations with numerical simulations that smoothly switched between standing and traveling wave torques based on the maximal value of the wave shear $|k_r\xi_r|$ (Figure 5), with wave breaking leading to traveling waves for $|k_r\xi_r| \gtrsim 1$ (§ 6.1). We presented the results of two simulations, one with a helium WD and one with a carbon/oxygen WD, in § 8. Once the traveling wave resonance lock began, synchronization in our numerical calculations proceeded until the spin frequency $\Omega_{\rm spin}$ became larger than $\delta\Omega = \Omega - \Omega_{\rm spin}$, meaning nonlinear rotational effects not included in our analysis were likely to be important (§ 9.2).

Our numerical calculations (Figure 6) demonstrate that efficient tidal dissipation is produced by standing wave resonance locks at large orbital periods, and by traveling wave resonance locks at smaller orbital periods. The importance of the standing wave resonance lock regime at large orbital periods can be tested by measuring the rotation rates of wide WD binaries. We predict that systems with orbital periods of hours should have undergone significant synchronization (Figure 6), while models that focus solely on excitation of traveling waves (Fuller & Lai 2012) would predict synchronization only at significantly shorter orbital periods. A second prediction of our model is that there may be a range of intermediate orbital periods (e.g., 20 min $\lesssim P_{\rm orb} \lesssim$ 40 min) where tidal dissipation is relatively inefficient compared to both smaller and somewhat larger orbital periods.

The results derived here can be directly compared to the recently discovered 13-minute WD binary J0651 (§ 9.1). We predict a $\sim 3\%$ deviation of the orbital decay rate from the purely gen-

eral relativistic value, which may be measurable given further observations. We also find that our predicted tidal heating rates are within an order of magnitude of the observed luminosities. This broad agreement is encouraging given the well-known difficulties tidal theory has accurately predicting the efficiency of tidal dissipation in many stellar and planetary systems.

In detail, we find that even if the helium WD is nonrotating (which maximizes the tidal energy dissipated as heat), tidal heating is a factor of ~ 2 less than the observed luminosity, strongly suggesting that much of its luminosity must derive from residual nuclear burning or cooling of thermal energy rather than tidal heating. In contrast, we predict that the carbon/oxygen WD in J0651 should be ~ 10 times more luminous than is observed. We suspect that the origin of this discrepancy is the importance of rotational modification of stellar eigenmodes at the short orbital period present in J0651 (§ 9.2), and perhaps the effects of nonlinear damping/excitation of stellar oscillations (e.g. § 9.4; Weinberg et al. 2012). These will be studied in future work.

ACKNOWLEDGMENTS

J.B. thanks Jieun Choi for assistance in the preparation of this manuscript. This work was supported by NSF AST-0908873 and NASA NNX09AF98G. J.B. is an NSF Graduate Research Fellow. E.Q. was supported by a Simons Investigator award from the Simons Foundation, the David and Lucile Packard Foundation, and the Thomas Alison Schneider Chair in Physics at UC Berkeley. P.A. is an Alfred P. Sloan Fellow, and received support from the Fund for Excellence in Science and Technology from the University of Virginia.

APPENDIX A: ANGULAR MOMENTUM TRANSPORT

If we assume there is a source of angular momentum near the WD surface, e.g. from tides, a fossil magnetic field of initial magnitude $\sim B_0$ will wind up and exert magnetic tension forces attempting to enforce solid-body rotation. The rate at which magnetic tension transports polar angular momentum through a spherical surface S at radius r is given by

$$\dot{J_z} = \frac{1}{4\pi}\int_S B_r B_\phi \, r \sin\theta \, dS, \tag{A1}$$

which can be derived by applying the divergence theorem to the magnetic tension force density $(\mathbf{B}\cdot\boldsymbol{\nabla})\mathbf{B}/4\pi$. As the field winds up, the radial component remains constant, while the azimuthal component increases as (Spruit 1999)

$$B_\phi = N_\mathrm{w} B_r, \tag{A2}$$

where $N_\mathrm{w} = r\sin\theta\int(d\Omega_\mathrm{spin}/dr)dt$ is the rotational displacement that occurs during wind up and we have assumed the rotational velocity field can be described by "shellular" rotation: $\mathbf{v} = \Omega_\mathrm{spin}(r) r\sin\theta\hat{\phi}$.

Once the field wind up propagates into the WD core, an equilibrium field is established that communicates the tidal torque throughout the WD and eliminates any rotational shear. There are several requirements necessary for this equilibrium to be reached during inspiral, and consequently for WDs in inspiraling binaries to rotate as a rigid bodies.

A1 Solid-body rotation at short orbital periods

Whether there is sufficient time for the global equilibrium magnetic field to develop and eliminate differential rotation altogether amounts to whether the timescale over which the torque changes, given by the gravitational wave inspiral time t_gw (equation 1), is longer than the timescale over which the wind up of the magnetic field propagates into the core, which is given by the global Alfvén crossing time $\langle t_\mathrm{A}\rangle = \int dr/v_\mathrm{A}$, where $v_\mathrm{A} = B_r/\sqrt{4\pi\rho}$ is the radial Alfvén speed. This restriction translates to

$$B_0 \gg \frac{1}{t_\mathrm{gw}}\int_0^R \sqrt{4\pi\rho}\, dr, \tag{A3}$$

where we have assumed $B_r \sim B_0 \sim$ constant. We can evaluate this further as

$$B_0 \gg 0.2\ \mathrm{G}\left(\frac{P_\mathrm{orb}}{10\ \mathrm{min}}\right)^{-8/3} F_1 \tag{A4}$$

where

$$F_1 = \left(\frac{M'}{M}\right)\left(\frac{1+M'/M}{2}\right)^{-1/3}\left(\frac{M}{0.60M_\odot}\right)^{13/6}\left(\frac{R}{0.013R_\odot}\right)^{-1/2}.$$

The other requirement for solid-body rotation is that the rotational displacement N_w required for the equilibrium field configuration must not be too extreme, since the field becomes susceptible to resistive dissipation as well as various instabilities as it winds up (Spruit 1999). We can address this constraint by setting the tidal torque appropriate for a resonance lock $\tau_r = I_r\Omega/t_\mathrm{gw}$ (equation 9), where I_r is the moment of inertia up to a radius r, equal to equation (A1), and then requiring $N_\mathrm{w} \lesssim 1$. Solving for B_0, we have

$$B_0 \gtrsim \sqrt{\frac{\tau}{r^3}} = \sqrt{\frac{I_r\Omega}{r^3 t_\mathrm{gw}}}. \tag{A5}$$

Since the right-hand side of equation (A5) scales radially as r^1, we can safely set $I_r = I_*$ and $r = R$. Evaluating this further yields

$$B_0 \gtrsim 10^4\ \mathrm{G}\left(\frac{P_\mathrm{orb}}{10\ \mathrm{min}}\right)^{-11/6} F_2, \tag{A6}$$

where

$$F_2 = \left(\frac{M'}{M}\right)^{1/2}\left(\frac{1+M'/M}{2}\right)^{-1/6}\left(\frac{I_*}{0.18MR^2}\right)^{1/2}\left(\frac{M}{0.6M_\odot}\right)^{4/3}\left(\frac{R}{0.013R_\odot}\right)^{-1/2}. \tag{A7}$$

We see that equation (A4) is likely to hold nearly until mass transfer, meaning there is always sufficient time to set up an equilibrium field capable of stably transmitting angular momentum throughout the WD and enforcing solid-body rotation. Equation (A6) is more restrictive, however, and shows that even for a fossil field of initial magnitude of $B_0 \sim 10^6$ G in a carbon/oxygen WD (§ 6.2), excessive wind up may begin to occur below an orbital period of ~ 1 min. Nonetheless, at orbital periods of ~ 100 min where standing-wave resonance locks occur, which require solid-body rotation, equation (A6) requires only modest fields of ~ 200 G.

Lastly, although angular momentum transport occurs due to a wound-up equilibrium magnetic field, torsional Alfvén waves can also be excited, which cause oscillations in the differential rotation profile. Formally, a phase-mixing timescale must elapse before such waves damp (Spruit 1999). However, due to the slowly varying torque, we expect Alfvén wave excitation to be weak. Indeed, in simulations of the solar magnetic field's evolution, Charbonneau & MacGregor (1993) found that Alfvén wave amplitudes (in terms of $\delta\Omega_\mathrm{spin}/\Omega_\mathrm{spin}$) were small.

A2 Transport during an initial resonance lock

When a standing wave resonance lock first begins to takes hold, angular momentum is applied exclusively to a thin layer near the outer wave turning point where wave damping predominantly occurs. Since no equilibrium field state has yet developed in this situation, a concern exists that the layer will rapidly synchronize and destroy the lock before it begins (§ 6.2).

To this end, we first compare the spin-up timescale of the layer to the Alfvén travel time t_A across it. Using the torque for a resonance lock from equation (9) and taking $t_A = H/v_A$, where H is the thickness of the layer, we have

$$\frac{(2/3)4\pi\rho r^4 H\Omega_{\rm spin}}{I_*\Omega_{\rm spin}/t_{\rm gw}} \gg \frac{H\sqrt{4\pi\rho}}{B_r}. \tag{A8}$$

Evaluating ρ at the radiative-convective boundary (RCB), letting $B_r \sim B_0$, and setting $r \approx R$, this becomes

$$B_0 \gg \sqrt{\frac{4\pi}{\rho_{\rm rcb}}}\left(\frac{3I_*}{8\pi R^4 t_{\rm gw}}\right). \tag{A9}$$

We can evaluate this further as

$$B_0 \gg 10^{-3}\ {\rm G}\left(\frac{P_{\rm orb}}{200\ {\rm min}}\right)^{-8/3} F_3, \tag{A10}$$

where

$$F_3 = \left(\frac{\rho_{\rm rcb}}{8.4\times10^{-7}\rho_{\rm c}}\right)^{-1/2}\left(\frac{M'}{M}\right)\left(\frac{1+M'/M}{2}\right)^{-1/3}\left(\frac{I_*}{0.18MR^2}\right)\left(\frac{M}{0.60M_\odot}\right)^{13/6}\left(\frac{R}{0.013R_\odot}\right)^{-1/2}$$

and $\rho_{\rm c}$ is the central density.

Secondly, even if no critical layer occurs, it is still necessary for the *global,* wound-up equilibrium field to develop quickly in order for an initial resonance lock to develop. Specifically, in order for a particular resonance to halt the increase in the tidal driving frequency $\sigma = 2(\Omega - \Omega_{\rm spin})$, its locally applied tidal torque must be communicated globally fast enough relative to the timescale over which the torque changes significantly. If this cannot occur, the system sweeps through the resonance without locking (see also § 6.3). The timescale over which a maximally resonant torque decays by roughly a factor of two is given by the time for the detuning $\delta\omega$ to increase from zero to of order the associated mode's damping rate γ_n (see e.g. equation 5; also Appendix B3). Comparing to the global Alfvén travel time $\langle t_A\rangle$, this condition becomes

$$B_0 \gg \frac{\Omega}{\gamma_n t_{\rm gw}}\int_0^R \sqrt{4\pi\rho}\, dr, \tag{A11}$$

which is identical to equation (A3) except with an additional factor of Ω/γ_n on the right-hand side. Evaluating further, we have

$$B_0 \gg 100\ {\rm G}\left(\frac{P_{\rm orb}}{200\ {\rm min}}\right)^{-11/3}\left(\frac{\gamma_n^{-1}}{120\ {\rm yr}}\right) F_1, \tag{A12}$$

where F_1 was defined in Appendix A1. The value of 100 G reduces to 6 G for a helium WD (`He7` from Table 1), holding γ_n constant. This is a much stricter requirement than equation (A10), but still seems likely to be satisfied given typical WD fields (§ 6.2).

APPENDIX B: GLOBAL NORMAL MODE ANALYSIS

B1 Mode dynamics

Here we give an overview of linear normal mode analysis as it applies to tidal interactions. As such, we assume the fluid motions generated by the tidal potential represent standing waves; we discuss the possibility of traveling waves in § 7.

In linear perturbation theory, we expand all fluid variables in spherical harmonics angularly, indexed by l and m, and adiabatic normal modes radially, indexed by the number of radial nodes n, as

$$\delta X(r,\theta,\phi,t) = \sum_{l=2}^{\infty}\sum_{m=-l}^{l}\sum_{n} q_{nlm}(t)\delta X_{nlm}(r)Y_{lm}(\theta,\phi). \tag{B1}$$

We computed normal modes using the ADIPLS stellar pulsation package (Christensen-Dalsgaard 2008). In this work we concern ourselves only with quadrupolar eigenmodes, and consider only circular orbits, meaning we can let $l = 2$ and $m = \pm 2$, since $m = 0$ modes have no time dependence with zero eccentricity. Thus equation (B1) becomes

$$\delta X(r,\theta,\phi,t) = 2\sum_{n}{\rm Re}\left[q_n(t)\delta X_n(r)Y_{22}(\theta,\phi)\right], \tag{B2}$$

with $m = 2$ used throughout.

We can write the momentum equation schematically as (Press & Teukolsky 1977)

$$\rho\ddot{\boldsymbol{\xi}} = -\rho\mathcal{L}[\boldsymbol{\xi}] - \rho\nabla U, \tag{B3}$$

where the linear internal acceleration operator $\mathcal{L}$ satisfies $\mathcal{L}[\boldsymbol{\xi}_n] = \omega_n^2\boldsymbol{\xi}_n$, ω_n is an eigenfrequency, and U is the tidal potential. The corotating

frame mode amplitude equations determining the behavior of each q_n can be obtained from equation (B3) by taking the scalar product with $\boldsymbol{\xi}_n^*$ on both sides and integrating over the star, yielding (e.g. Weinberg et al. 2012)

$$\ddot{q}_n + 2\gamma_n \dot{q}_n + \omega_n^2 q_n = 2\omega_n^2 \varepsilon W Q_n e^{-i\sigma t}, \tag{B4}$$

where $W = \sqrt{3\pi/10}$, $\varepsilon = (M'/M)(R/a)^3$ is the tidal factor, $\sigma = m(\Omega - \Omega_{\rm spin})$ is the tidal driving frequency, and the linear overlap integral Q_n is discussed in Appendix B4 (Press & Teukolsky 1977). We have also inserted into equation (B4) a damping rate γ_n, the calculation of which we describe in Appendix B3. We normalize our normal modes by setting

$$E_* = E_n = \int_0^R 2\omega_n^2 \left(\xi_{r,n}^2 + l(l+1)\xi_{{\rm h},n}^2\right) \rho r^2 dr. \tag{B5}$$

Given slowly varying orbital and stellar properties, the steady-state solution to equation (B4) is

$$q_n(t) = 2\,\varepsilon\, Q_n W \left(\frac{\omega_n^2}{(\omega_n^2 - \sigma^2) - 2i\gamma_n\sigma}\right) e^{-i\sigma t}. \tag{B6}$$

The above amplitude applies in the corotating stellar frame; in the inertial frame the time dependence $e^{-i\sigma t}$ instead becomes $e^{-im\Omega t}$.

B2 Angular momentum and energy transfer

Assuming a circular orbit and alignment of spin and orbital angular momenta, the secular quadrupolar tidal torque on a star is given by an expansion in quadrupolar ($l = 2$) normal modes as (Burkart et al. 2012 Appendix C1 and references therein)

$$\tau = 8mE_*\varepsilon^2 W^2 \sum_n Q_n^2 \frac{\omega_n^2 \sigma\gamma_n}{(\omega_n^2 - \sigma^2)^2 + 4\sigma^2\gamma_n^2}, \tag{B7}$$

where most variables are defined in the previous section.

The tidal energy deposition rate into the star $\dot{E}_{\rm tide}$ can be determined from τ by the relation

$$-\dot{E}_{\rm orb} = \dot{E}_{\rm tide} = \Omega\,\tau, \tag{B8}$$

valid only for a circular orbit. This can be derived by differentiating standard equations for the energy and angular momentum of a binary with respect to time, setting $\dot{e} = e = 0$, and noting that the tidal torques and energy deposition rates in each star of a binary are independent.

The total energy contained in the linear tide can be expressed in the corotating frame as (Schenk et al. 2002)

$$E_{\rm tide} = \frac{1}{2}\left\langle \dot{\boldsymbol{\xi}}, \dot{\boldsymbol{\xi}} \right\rangle + \frac{1}{2}\left\langle \boldsymbol{\xi}, \mathcal{L}[\boldsymbol{\xi}] \right\rangle, \tag{B9}$$

where the operator $\mathcal{L}$ was introduced in Appendix B1. Using results from Appendix B1, we can evaluate this expression as

$$E_{\rm tide} = 2E_*\varepsilon^2 W^2 \sum_n Q_n^2 \frac{\omega_n^2(\sigma^2 + \omega_n^2)}{(\omega_n^2 - \sigma^2)^2 + 4\sigma^2\gamma_n^2}. \tag{B10}$$

Lastly, since the great majority of the tidal energy is in the lowest-order modes, i.e. the equilibrium tide, which satisfy $\omega_n \gg \sigma$, we can further set $\sigma \approx 0$ in the previous equation to derive the simple expression

$$E_{\rm tide} \approx \lambda E_* \varepsilon^2, \tag{B11}$$

where

$$\lambda = 2W^2 \sum_n Q_n^2. \tag{B12}$$

Several limits can be taken of our general torque expression in equation (B7). First, if we assume $\omega_n \gg (\sigma, \gamma_n)$, we arrive at the equilibrium tide limit:

$$\tau_{\rm eq} = 8mE_*\varepsilon^2 W^2 \sum_n Q_n^2 \left(\frac{\sigma\gamma_n}{\omega_n^2}\right). \tag{B13}$$

Willems et al. (2010) showed that in linear theory the equilibrium tide provides a negligible torque due to the very weak damping present in WDs, resulting from their high densities and long thermal times. We confirm this result: e.g., the tidal quality factor associated with damping of the quadrupolar equilibrium tide in WDs is (equation 15)

$$\mathcal{Q}_{\rm t}^{\rm eq} = \frac{1}{8}\frac{\sum_n Q_n^2}{\sum_n Q_n^2 \sigma\gamma_n/\omega_n^2} \gtrsim 10^{13}, \tag{B14}$$

which is much larger than the effective value of $\mathcal{Q}_{\rm t}$ for the dynamical tide determined in § 5.1. The resonant dynamical tide ($\omega_n \sim \sigma$ in equation B7) is discussed in §§ 4 & 7.

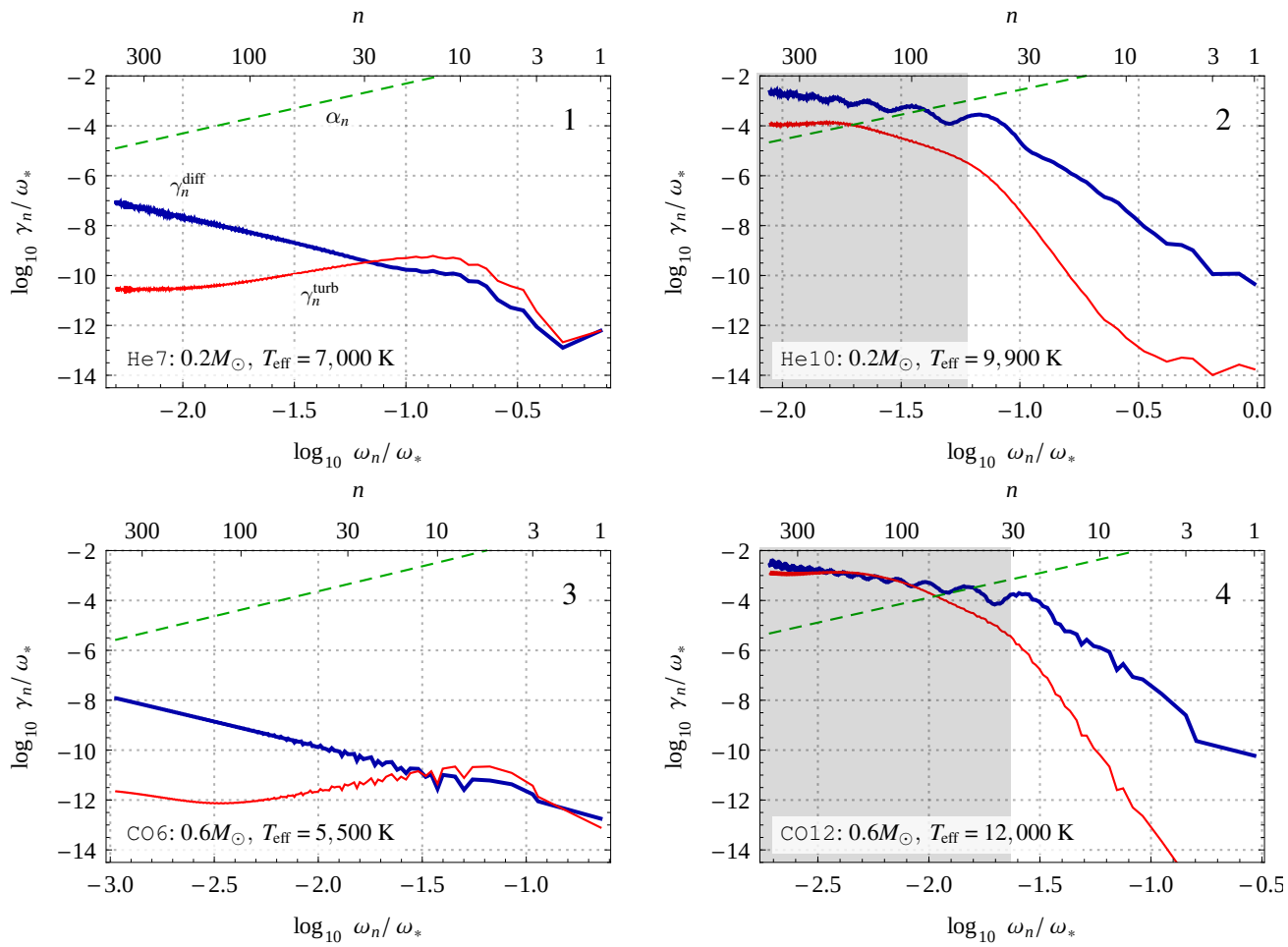

Figure B1. Plots of the contributions to eigenmode damping rates due to thermal diffusion $\gamma_n^{\rm diff}$ (thick blue lines) and turbulent convection $\gamma_n^{\rm turb}$ (red lines), as well as the effective damping rate for traveling waves $\alpha_n = 2\pi/t_{{\rm group},n}$ (dashed green lines), as functions of the eigenmode frequency ω_n (in units of the dynamical frequency ω_*) and radial order n, for the first 400 g-modes in four of our fiducial WD models (Table 1). We describe the computation of these quantities in Appendix B3. Inside the shaded regions in panels 2 & 4, g-modes become traveling waves due to rapid thermal diffusion near their outer turning points. In this case, approximating wave damping rates using $\gamma_n^{\rm diff} + \gamma_n^{\rm turb}$ is invalid, and a traveling wave formalism such as that discussed in § 7 must be used. Note that the WD models shown here are different from those in Figure 4.

B3 Damping

We consider two different damping processes in this appendix: thermal diffusion and turbulent convection. We also calculate g-modes' group travel times, which sets the effective damping time for traveling waves. Figure B1 shows plots of all three of these quantities for several of our fiducial WD models, and demonstrates that thermal diffusion is the dominant source of damping for high-order g-modes in WDs.

Damping due to electron conduction and radiative diffusion can be estimated simultaneously as (Goodman & Dickson 1998)

$$\gamma_n^{\rm diff} = \frac{1}{2E_n} \int \chi k_r^2 \frac{dE_n}{dr} dr, \tag{B15}$$

where dE_n/dr is the integrand of equation (B5), χ is the thermal diffusivity (including both radiative diffusion and electron conduction), and k_r is the radial wavenumber. In terms of an effective opacity κ, χ can be expressed as

$$\chi = \frac{16\sigma T^3}{3\kappa\rho^2 c_p}. \tag{B16}$$

For high-order g-modes, k_r is given by (Christensen-Dalsgaard 2008)

$$k_r^2 = k_{\rm h}^2 \left(\frac{N^2}{\omega^2} - 1 \right), \tag{B17}$$

where $k_{\rm h}^2 = l(l+1)/r^2$ is the angular wavenumber. The integration in equation (B15) is performed up to the adiabatic cutoff radius defined by $\omega t_{\rm th} = 1$ (Unno et al. 1989), where $t_{\rm th} = pc_pT/gF$ is the local thermal time. A wave's group travel time across a scale height must remain smaller than its local damping time in order for the wave to reflect. This criterion will always be broken for sufficiently long-period waves

since the radial wavenumber k_r grows as ω^{-1}; nonetheless, we find that thermal diffusion is never strong enough to invalidate the standing wave assumption for all of the modes used in this work that are capable of effecting standing wave resonance locks.

To estimate the turbulent convective damping rate, we rely on the calibration of convective viscosity performed by Penev et al. (2009). The formula we employ is

$$\gamma_n^{\rm turb} \sim \frac{\omega_n^2}{E_n}\int \rho r^2 \nu_{\rm turb}\left[s_{0'}\left(\frac{d\xi_r}{dr}\right)^2 + s_1 l(l+1)\left(\frac{d\xi_{\rm h}}{dr}\right)^2\right]dr, \tag{B18}$$

where $s_{0'} = 0.23$ and $s_1 = 0.084$ (Penev & Sasselov 2011). For the effective turbulent viscosity $\nu_{\rm turb}$, we use equation (11) of Shiode et al. (2012):

$$\nu_{\rm turb} = L v_{\rm conv} \min\left[\frac{1}{\Pi_{\rm min}}\left(\frac{2\pi}{\omega t_{\rm eddy}}\right)^2, \left(\frac{2\pi}{\omega t_{\rm eddy}}\right), \Pi_{\rm max}\right], \tag{B19}$$

where $v_{\rm conv}$ is the convective velocity, L is the mixing length, $t_{\rm eddy} = v_{\rm conv}/L$, $\Pi_{\rm min} = 0.1$, and $\Pi_{\rm max} = 2.4$.

Lastly, the effective damping rate applicable in the traveling wave regime is the inverse group travel time $\alpha = 2\pi/t_{\rm group}$; we can calculate $t_{\rm group}$ as

$$t_{\rm group} = 2\int \frac{dr}{|v_{\rm group}|}, \tag{B20}$$

where $v_{\rm group} = d\omega/dk_r$ and the integration is over the propagation cavity where the wave frequency $\omega < N$. Using the dispersion relation from equation (B17), this becomes

$$\alpha = \pi\left(\int \frac{k_{\rm h} N}{\omega^2} dr\right)^{-1}. \tag{B21}$$

For $\omega \ll N$, $\alpha \propto \omega^2$; this proportionality is verified in Table 3 and Figure B1.

B4 Linear overlap integral

The linear overlap integral for quadrupolar eigenmodes, introduced in equation (B4), can be expressed as

$$\begin{aligned} Q_n &= \frac{1}{MR^l}\int_0^R l\left(\xi_{r,n} + (l+1)\xi_{{\rm h},n}\right)\rho r^{l+1} dr \\ &= \frac{1}{MR^l}\int_0^R \delta\rho_n\, r^{l+2} dr \\ &= -\frac{R}{GM}\cdot\frac{2l+1}{4\pi}\cdot\delta\phi_n(R), \end{aligned} \tag{B22}$$

with $l = 2$, where $\xi_{\rm h}$ is the horizontal fluid displacement. The second equality can be derived by substituting the continuity equation, and the third equality by substituting Poisson's equation. However, all three of these methods of calculating Q_n suffer from numerical difficulties, presumably arising due to a failure of orthogonality or completeness of the numerically computed eigenmodes (Fuller & Lai 2011), or to small inconsistencies in the stellar model (Fuller & Lai 2012).

Thus we now consider a more stable way of numerically evaluating Q_n, which is what we actually employed in our calculations and the fits in Table 3. We again focus on $l = 2$ modes, but the technique can easily be extended to arbitrary l. First, the tidally generated displacement field is given as a sum of normal modes in equation (B1). If we set the tidal driving frequency σ and the damping rate γ_n to zero in equation (B6) and substitute into equation (B2) (while keeping the tidal factor ε nonzero), we recover the equilibrium tide limit. However, the equilibrium tide can alternatively be obtained by directly solving the inhomogeneous linear stellar oscillation equations in the zero-frequency limit; see e.g. Weinberg et al. (2012) Appendix A.1. Equating these two alternate expressions, taking the scalar product with $\rho\boldsymbol{\xi}_n^*$ on both sides, integrating over the star, and solving for Q_n, one obtains

$$Q_n = \frac{\omega_n^2}{WE_*}\int_0^R \left(X_{\rm eq}^r \xi_n^r + l(l+1) X_{\rm eq}^{\rm h} \xi_n^{\rm h}\right)\rho r^2 dr, \tag{B23}$$

where

$$\mathbf{X}_{\rm eq}(r,\theta,\phi) = \sum_{m=\pm 2}\left(X_{\rm eq}^r(r)\hat{r} + r X_{\rm eq}^{\rm h}(r)\boldsymbol{\nabla}\right) Y_{2m}(\theta,\phi) \tag{B24}$$

is the numerically computed $l = 2$ equilibrium tide scaled to $\varepsilon = 1$.

Finally, there is one further method of computing Q_n that we have employed, which also uses a solution to the inhomogeneous equations. In this method, however, instead of comparing alternate computations of the equilibrium tide, we instead evaluate the inhomogeneous tidal response very near an eigenfrequency. The overlap can then be extracted by fitting the resulting Lorentzian profile of e.g. the tidal energy. This method numerically agrees very well with the equilibrium tide method described above.

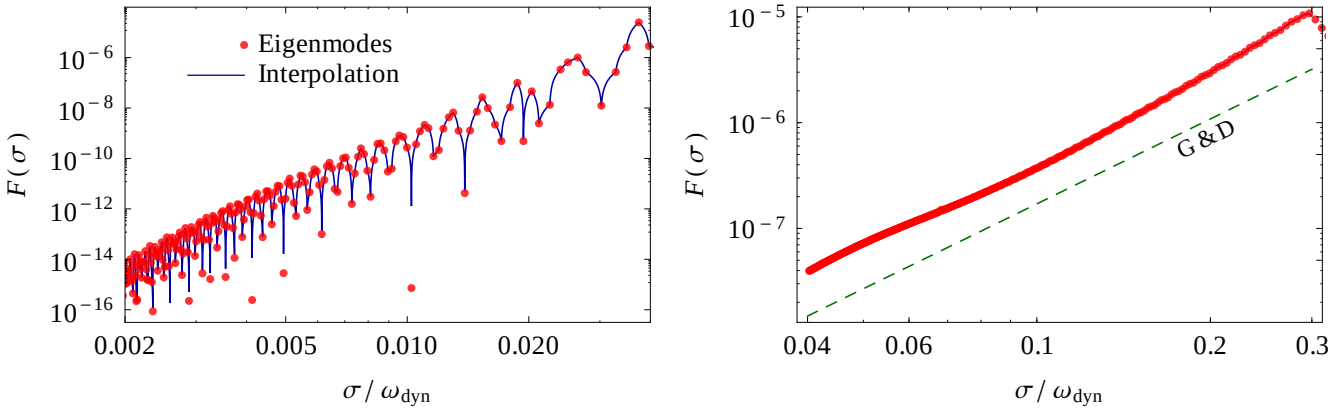

Figure C1. Dimensionless traveling wave tidal torque $F(\sigma) = \tau_{\rm trav}/\varepsilon^2 E_*$, computed as described in § 7.2. Red points show direct evaluations of equation (32) at eigenmode frequencies, while blue lines are linear interpolations of these values. *Left panel:* Results for our $0.6 M_\odot$, $T_{\rm eff} = 5,500$ K `CO6` WD model (Table 1). To facilitate straightforward comparison, this plot employs the same axes and conventions as in Figure 8 of Fuller & Lai (2012). *Right panel:* Results for a solar model, which agrees reasonably well with the semi-analytic traveling wave result in equation (13) of Goodman & Dickson (1998) (dashed green line).

APPENDIX C: VERIFICATION OF TRAVELING WAVE TORQUE APPROXIMATION

Here we will justify our traveling wave tidal torque approximation described in § 7.2 using several distinct lines of reasoning. Our goal is to explain why the traveling wave torque can be expressed in terms of the properties of global eigenmodes as in equation (32). This is a different approach than is typical in the literature.

First, in the limit that the wave damping time is much longer than the group travel time, the tidal response is well approximated as a standing wave. Thus taking the standing wave torque and setting the damping rate equal to the inverse group travel time (Appendix B3) represents a natural method of smoothly transitioning to the traveling wave limit, since it corresponds to the situation where a wave is nearly completely absorbed over one travel time. One apparent difficulty with the resulting expression in our equation (32) is that it appears to contain explicit dependence on the wave travel time, which seems paradoxical, since a traveling wave has no information about the extent of the propagation cavity. This is, however, simply an artifact of our normalization convention. To show this, we first note that our approximation for $\tau_{\rm trav}$ depends on $\alpha = 2\pi/t_{\rm group}$ (Appendix B3) only through

$$\tau_{\rm trav} \propto Q^2/\alpha. \tag{C1}$$

Next, given the appropriate WKB expression for $\xi_{\rm h}$ (Christensen-Dalsgaard 2008),

$$\xi_{\rm h} \approx A\sqrt{\frac{N}{\rho r^3 \Lambda \sigma^3}}\sin\left(\int k_r dr + \delta\right), \tag{C2}$$

where A is a constant, we impose our normalization convention from equation (B5) and use the fact that $\xi_{\rm h} \gg \xi_r$ for g-modes to obtain

$$\begin{aligned} E_* &\approx 2\sigma^2 \int \Lambda^2 \xi_{\rm h}^2 \rho r^2 dr \\ &\approx A^2 \left(\frac{\pi\sigma\Lambda}{\alpha}\right), \end{aligned} \tag{C3}$$

having set $\sin^2 \to 1/2$. This implies that unnormalized eigenfunctions (which are independent of global integrals) must be multiplied by $A \propto \alpha^{1/2}$ in order to be normalized properly. Since the overlap integral Q is linear in the eigenfunctions (Appendix B4), re-examining equation (C1) shows that $\tau_{\rm trav}$ is indeed independent of α and hence $t_{\rm group}$.

An alternate justification of our traveling wave torque expression can be obtained by considering how a traveling wave of a given frequency σ can be expressed in terms of global standing wave eigenmodes, which form a complete basis (Dyson & Schutz 1979). Obtaining a traveling wave functional form of $e^{i(kr \pm \sigma t)}$ requires summing at least two real-valued eigenmodes with a relative global phase difference between their complex amplitudes of $\pm\pi/2$, where both modes possess frequencies close to σ. Examining equation (B6), we see that the phase of a standing mode's amplitude is given by $\arctan(\gamma/\delta\omega)$. Thus, in order to approximate a traveling wave of commensurate frequency, two adjacent eigenmodes 1 and 2 must satisfy

$$\arctan\left(\frac{\gamma_1}{\delta\omega_1}\right) - \arctan\left(\frac{\gamma_2}{\delta\omega_2}\right) = \pm\frac{\pi}{2}, \tag{C4}$$

which simplifies to $\gamma_1\gamma_2 = \delta\omega_1\delta\omega_2$. Setting $|\delta\omega_{1,2}| \approx (\Delta P_0/2\pi)\sigma^2 \approx \alpha$, where ΔP_0 is the asymptotic g-mode period spacing, we find that the damping rate required to produce a traveling wave is $\gamma \sim 2\pi/t_{\rm group}$, consistent with our equation (32).

Lastly, we will quantitatively demonstrate that our approximation for the traveling wave tidal torque reproduces results available in the literature. First, the left panel of Figure C1 shows our traveling wave torque evaluated for our `CO6` WD model (Table 1), expressed in the dimensionless form $F(\sigma) = \tau_{\rm trav}/\varepsilon^2 E_*$, as a function of the $l = m = 2$ tidal forcing frequency $\sigma = 2(\Omega - \Omega_{\rm spin})$. Comparing this to Figure 8 of Fuller & Lai (2012), which employs the same conventions and axes, shows reasonable agreement. In particular, both exhibit the jagged

variation with frequency discussed in § 7.1. Our result has a slightly steeper overall trend, leading to a smaller torque at low frequencies; however, because excitation is sensitive to the details of the composition boundaries in the model, there is no reason to expect detailed agreement. In addition, the right panel of Figure C1 compares traveling wave results for solar-type stars from Goodman & Dickson (1998) (using their equation 13) with our equation (32) applied to a solar model. Both possess the same power-law scaling with frequency, and agree in normalization within a factor of ~ 2.

APPENDIX D: WHITE DWARF MODELS

We used MESA version 4298 (Paxton et al. 2011) to produce our helium WD models (Table 1: `He5`, `He7`, and `He10`). We used three inlists. The first evolves a $1.6M_\odot$ star with $Z = 0.02$ from ZAMS to where $0.198M_\odot$ of its core is locally at least 90% helium. Salient non-default parameter values are:

```
mesh_delta_coeff = 0.5
h1_boundary_limit = 0.1
h1_boundary_mass_limit = 0.198
```

The second smoothly removes the outer $1.4M_\odot$, leaving a hydrogen layer with $\sim 1\%$ of the remaining mass. This is achieved with:

```
relax_mass = .true.
new_mass = 0.2
```

The third evolves the resulting $0.2M_\odot$ WD until $T_{\rm eff} = 5{,}000$ K. We invoke MESA's element diffusion routine even where the plasma interaction parameter $\Gamma > 1$. Salient non-default parameter choices are:

```
mesh_delta_coeff = 0.05
which_atm_option = 'simple_photosphere'
surf_bc_offset_factor = 0
do_element_diffusion = .true.
use_Ledoux_criterion = .true.
diffusion_gamma_full_off = 1d10
diffusion_gamma_full_on = 1d10
diffusion_T_full_off = -1
diffusion_T_full_on = -1
diffusion_Y_full_off = -1
diffusion_Y_full_on = -1
```

Our carbon/oxygen WD models (Table 1: `CO6` and `CO12`) were produced by solving for hydrostatic equilibrium subject to heat transport by radiative diffusion and electron conduction (Hansen et al. 2004). We use the OPAL EOS and effective opacities (Rogers et al. 1996) in the WD outer layers, and transition to the Potekhin-Chabrier EOS and electron conduction opacities (Potekhin & Chabrier 2010) where the electrons begin to become degenerate. We use a mixture of 25% carbon, 75% oxygen for the inner 98% of the model's mass, then add a helium layer with 1.7% of the mass, and finally a hydrogen layer with the remaining 0.17%. We smooth the composition transition regions over $\sim 0.1H_p$ with a Gaussian profile, where H_p is a pressure scale height. We treat convection with mixing length theory, using $L = H_p$ for the mixing length.

REFERENCES

Arras P., Flanagan E. E., Morsink S. M., Schenk A. K., Teukolsky S. A., Wasserman I., 2003, ApJ, 591, 1129
Barker A. J., Ogilvie G. I., 2010, MNRAS, 404, 1849
Brown W. R., Kilic M., Hermes J. J., Allende Prieto C., Kenyon S. J., Winget D. E., 2011, ApJL, 737, L23
Burkart J., Quataert E., Arras P., Weinberg N. N., 2012, MNRAS, 421, 983
Campbell C. G., 1984, MNRAS, 207, 433
Charbonneau P., MacGregor K. B., 1993, ApJ, 417, 762
Christensen-Dalsgaard J., 2008, Ap&SS, 316, 113
Dewitt H., Slattery W., Baiko D., Yakovlev D., 2001, Contributions to Plasma Physics, 41, 251
Dyson J., Schutz B. F., 1979, Royal Society of London Proceedings Series A, 368, 389
Fuller J., Lai D., 2011, MNRAS, 412, 1331
Fuller J., Lai D., 2012, MNRAS, 421, 426
Goldreich P., Nicholson P. D., 1989a, ApJ, 342, 1079
Goldreich P., Nicholson P. D., 1989b, ApJ, 342, 1075
Goldreich P., Soter S., 1966, *Icarus*, 5, 375

Goodman J., Dickson E. S., 1998, ApJ, 507, 938
Hansen C. J., Kawaler S. D., Trimble V., 2004, Stellar Interiors, 2nd edn. Springer, New York
Hansen C. J., van Horn H. M., 1979, ApJ, 233, 253
Hermes J. J. et al., 2012, ApJL, 757, L21
Horowitz C. J., Berry D. K., Brown E. F., 2007, Phys. Rev. E, 75, 066101
Iben, Jr. I., Tutukov A. V., Fedorova A. V., 1998, ApJ, 503, 344
Liebert J., Bergeron P., Holberg J. B., 2003, AJ, 125, 348
Lindzen R. S., 1981, J. Geophys. Res., 86, 9707
Panei J. A., Althaus L. G., Chen X., Han Z., 2007, MNRAS, 382, 779
Paxton B., Bildsten L., Dotter A., Herwig F., Lesaffre P., Timmes F., 2011, ApJS, 192, 3
Penev K., Barranco J., Sasselov D., 2009, ApJ, 705, 285
Penev K., Sasselov D., 2011, ApJ, 731, 67
Peters P. C., 1964, Physical Review, 136, 1224
Piro A. L., 2011, ApJL, 740, L53
Potekhin A. Y., Chabrier G., 2010, Contributions to Plasma Physics, 50, 82
Press W. H., Teukolsky S. A., 1977, ApJ, 213, 183
Rathore Y., Blandford R. D., Broderick A. E., 2005, MNRAS, 357, 834
Rogers F. J., Swenson F. J., Iglesias C. A., 1996, ApJ, 456, 902
Schenk A. K., Arras P., Flanagan É. É., Teukolsky S. A., Wasserman I., 2002, PhRvD, 65, 024001
Shiode J. H., Quataert E., Arras P., 2012, MNRAS, 423, 3397
Spruit H. C., 1999, A&A, 349, 189
Thompson T. A., 2011, ApJ, 741, 82
Unno W., Osaki Y., Ando H., Saio H., Shibahashi H., 1989, Nonradial Oscillations of Stars. Tokyo University Press, Japan
Weinberg N. N., Arras P., Quataert E., Burkart J., 2012, ApJ, 751, 136
Willems B., Deloye C. J., Kalogera V., 2010, ApJ, 713, 239
Winget D. E., Kepler S. O., Campos F., Montgomery M. H., Girardi L., Bergeron P., Williams K., 2009, ApJL, 693, L6
Witte M. G., Savonije G. J., 1999, A&A, 350, 129
Zahn J.-P., 1975, A&A, 41, 329
Zahn J.-P., 1977, A&A, 57, 383